

TOP-DOWN CONSTRAINING THE ESTIMATES OF ANTHROPOGENIC AEROSOL
EMISSIONS AND THE PARAMETERIZATION OF DUST SOURCES

by

Xiaoguang Xu

A DISSERTATION

Presented to the Faculty of
The Graduate College at the University of Nebraska

In Partial Fulfilment of Requirements

For the Degree of Doctor of Philosophy

Major: Earth & Atmospheric Sciences
(Meteorology/Climatology)

Under the Supervision of Professor Jun Wang

Lincoln, Nebraska

May, 2015

Table of Contents

List of Figures	v
List of Tables	viii
1 Introduction	1
1.1 Background and Motivation	1
1.1.1 Top-down versus bottom-up	2
1.1.2 Satellite Observations of Aerosol	5
1.2 Main Goals of This Work	5
1.3 Organization of This Dissertation	7
2 Top-Down Inversion Framework	8
2.1 Inversion Theory and Infrastructure	8
2.2 GEOS-Chem Forward Modeling	11
2.2.1 Anthropogenic aerosol emissions	11
2.2.2 Dust emissions	11
2.3 GEOS-Chem Adjoint Modeling	12
3 Optimizing Species-Specified Aerosol Emissions	14
3.1 Introduction	14

3.2	Constraints from Satellite Radiances	16
3.3	Inversion Strategies	18
3.3.1	Selection of emissions for optimization	18
3.3.2	Sensitivity test with pseudo AOD observations	19
3.4	Inversion Results	21
3.5	Results Evaluations	27
3.5.1	Comparison with AERONET AOD	27
3.5.2	Comparison with MISR AOD	29
3.5.3	Comparisons with OMI Column SO ₂ and NO ₂	31
3.5.4	Comparisons with near-surface aerosol mass concentrations	32
3.5.5	Evaluation summary	34
3.6	Implications of Results	37
3.6.1	SO ₂	37
3.6.2	NH ₃	39
3.6.3	NO _x	39
3.6.4	BC and OC	39
3.6.5	Mineral dust	40
3.7	Summary	41
4	Optimizing Dust Source Parameterization	45
4.1	Introduction	45
4.2	Necessary Implementations	46
4.2.1	Development of the wind speed distribution	46
4.2.2	AOD observation operator	49
4.2.3	Adjoint for Dust Flux Parameterization	49
4.3	Constraints from Multi-Satellite Observations	50

4.4	Experiment Design	50
4.5	Constrained Dust Emission Scheme	50
4.6	Validations	50
4.7	Summary	50
5	Summary and Outlook	51
5.1	Summary of the Dissertation	51
5.2	Main Conclusions of This Work	51
5.3	Outlook and Future Work	51
A	Abbreviations and Acronyms	52
B	Symbols	53
	References	54
	List of Publications	58

List of Figures

3.1	Flowchart of the proposed top-down inversion framework.	15
3.2	Relative changes in posterior aerosol emissions from <i>a priori</i> in the pseudo-observation experiment. Six panels are respectively for anthropogenic emissions of SO ₂ , NH ₃ , NO _x , BC, and OC, and mineral dust from both natural and anthropogenic sources. The red box in panel (a) indicates the region where AOD observations are selected.	20
3.3	Comparison of the prior (a) and posterior (b) GEOS-Chem (GC) simulation of 0.65 μ m AOD with the AOD at the same wavelength retrieved from MODIS reflectance using GEOS-Chem aerosol optical properties (c) averaged for the period of April 2008. Satellite retrievals with 10 km by 10 km at nadir are aggregated to GEOS-Chem grid cells; and the model AOD are sampled coincidentally with those retrievals. Panel (d) and (e) respectively show the difference of prior and posterior simulated from the satellite retrieved AODs. The red box in panel (c) indicates the region where AOD observations are selected.	22
3.4	(a) Time series of the spatially averaged daily MODIS AOD retrievals (purple) for April 2008 over the Eastern China, compared by the prior (orange) and posterior (green) spatial averaged daily GEOS-Chem AOD that are sampled in the MODIS AOD tempo-spatial space. (b) Time series of the expected daily AOD adjustments (orange) that are the differences between MODIS AOD and the prior GEOS-Chem AOD and their real adjustments (green) that are the differences of posterior from prior GEOS-Chem AOD. (c) Time series of the prior (orange) and posterior (green) daily dust emissions over China for April 2008.	24

3.5	The prior (or bottom-up based, left column), optimized (or top-down constrained, middle column) aerosol emissions over China for the period of April 2008, and their relative differences (right column). Six rows from top to bottom are respectively for anthropogenic emissions of SO_2 , NH_3 , ceNO_x , BC, and OC, and mineral dust from both natural and anthropogenic sources.	25
3.6	(a – i) Scatterplots of GEOS-Chem AOD versus AERONET AOD at $0.55 \mu\text{m}$ prior (red scatters) and posterior (green scatters) to the aerosol emission optimization over nine stations. AERONET AODs are 3-hour averages following the GEOS-Chem output frequency. (j) The overall comparison for eight AERONET sites excluding Beijing. Also shown are the number of valid sampled pairs (n), correlation coefficients (R), bias, and root-mean-square-error (rmse).	28
3.7	Comparison of the prior and posterior GEOS-Chem simulation of $0.55 \mu\text{m}$ AOD with the level 3 MISR $0.55 \mu\text{m}$ AOD for the period April 2008. (a) The prior GEOS-Chem $0.55 \mu\text{m}$ AOD that are sampled coincidentally with MISR AODs for the period of April 2008. Also overlaid circles are the monthly AOD averages at $0.55 \mu\text{m}$ observed from the nine AERONET sites shown in Figure 3.6. (b) Same as (a) but for the monthly average of posterior GEOS-Chem AOD. (c) Monthly average of the Level 3 daily MISR $0.55 \mu\text{m}$ AOD. (d) Scatter plot the GEOS-Chem AOD versus the MISR AOD before (red scatters) and after optimization (green scatters), in which each point indicates an AOD pair over a model grid cell with value over 0.2. Also shown are the statistics including number of sampled pairs (n), correlation coefficient (R), bias and root-mean-square-error (rmse). Comparisons of the monthly GEOS-Chem AOD versus AERONET AOD are also included as the black circles; each circle indicates an AOD pair over an individual site.	30
3.8	Same as figure 3.7 but for comparison of the GEOS-Chem SO_2 simulation with OMI column SO_2 retrievals for the period of April 2008. The OMI planetary boundary layer (PBL) column SO_2 from the Level 3 daily products with 0.25° by 0.25° resolutions are aggregated into GEOS-Chem grid cells.	32
3.9	Same figure 3.7 but for comparison of the GEOS-Chem NO_2 simulation with OMI column NO_2 retrievals for the period of April 2008. The OMI tropospheric column NO_2 from Level 2 daily products with 0.25° by 0.25° resolutions are aggregated into GEOS-Chem grid cells.	33

3.10	Comparison of the GEOS-Chem surface mass concentration of sulfate-nitrate-ammonium (SNA) aerosols with ground-based observations over Qingdao (120.34° E, 36.06° N), China. Discontinuity in time series is due to missing or quality filtered observations.	34
3.11	Time serial plot of the GEOS-Chem simulated surface PM ₁₀ concentrations by prior (red) and posterior (red) aerosol emissions compared with the <i>in situ</i> measured PM ₁₀ (black) over Zhangye (a) and SACOL (b) stations for 15 – 30 April 2008; also shown are the average values over same the period. Discontinuity in time series is due to missing or quality filtered observations.	35
3.12	Taylor diagram for the model evaluations before (squares) and after (circles) optimization when comparing against (1) AERONET AOD at 0.55 μ m, (2) MISR 0.55 μ m AOD, (3) OMI column SO ₂ , (4) OMI column NO ₂ , (5) surface SNA concentrations at Qingdao site, and (6) surface PM ₁₀ concentrations measured at Zhangye and SACOL sites. The color coded on each point indicates the relative bias. It should be noted that the ratio of standard deviations and correlation coefficient between prior GEOS-Chem simulated and measured surface PM ₁₀ over Zhangye and SACOL are 6.5 and 0.45, which makes the point number 6 for the prior simulation far beyond the range of this Taylor diagram.	36
3.13	Change of April monthly 0.55 μ m AOD from 2006 to 2008 from MODIS (a) and MISR (b) Level 3 daily products.	38

List of Tables

1.1	List of satellite sensors with measurement specifications relevant for operation retrieval of aerosol properties.	5
3.1	Prior, posterior, and perturbed aerosol emissions over China in the pseudo experiment.	21

CHAPTER 1

INTRODUCTION

1.1 Background and Motivation

Atmospheric aerosols play a crucial role in the global climate change. They affect earth energy budget directly by scattering and absorbing solar and terrestrial radiation, and indirectly through altering the cloud formation, lifetime, and radiative properties [Haywood and Boucher, 2000; Ramanathan et al., 2001]. However, quantification of these effects in the current climate models is fraught with uncertainties. The global average of aerosol effective radiative forcing (ERF) were estimated to range from -0.1 to -1.9 Wm² with the best estimate of -0.9 Wm² [Boucher et al., 2013], indicating that the cooling effects of aerosol might counteract the warming effects of 1.820.19 Wm² caused by the increase of carbon dioxide since the industrial revolution [Myhre et al., 2013]. The climate effects of aerosol particles depend on their geographical distribution, optical properties, and efficiency as cloud condensation nuclei (CCN). Key quantities pertain to the aerosol optical and cloud-forming properties include particle size distribution (PSD), chemical composition, mixing state, and morphology [Boucher et al., 2013]. While the daily aerosol optical depth (AOD) can be well measured from current satellite and ground-based remote sensing instrumentations [e.g., Holben et al., 1998; Kaufman et al., 2002], the accurate quantification of aerosol ERF is in no small part hindered by our limited knowledge about the aerosol PSD and refractive index (describing chemical composition and mixing state). To fully understand the role of

aerosol particles in the global climate change, further development in observations along with retrieval algorithms for these aerosol microphysical properties from different platforms are thus highly needed [Mishchenko et al., 2004], and the focus of this two-part series study is the characterization of aerosol properties from ground-based passive remote sensing [Henze et al., 2007].

Dust acts as medium in iron cycle on the earth [Jickells et al., 2005].

The long-distance transport of bacteria together with dust has been discussed in several studies as a mechanism for the global dispersion of microbial species, with the potential to impact ecosystems and public health [Griffin et al., 2001; Burrows et al., 2009]

In the following paragraphs of this section, I briefly describe the impacts of dust aerosols on the earth system, the basic physics of dust emissions, and the current state of satellite remote sensing of mineral dust. Subsequently, I present the specific scientific objectives and the organization of this thesis.

1.1.1 Top-down versus bottom-up

Current estimates of aerosol emissions are largely based on the “bottom-up” method that integrates diverse information such as fuel consumption in various industries and corresponding measurements of emission rates for different species [Streets et al., 2003], economic growth, and the statistics of land use and fire-burned areas [van der Werf et al., 2006]. While significant progress has been made [Streets et al., 2006], the “bottom-up” approach has a number of limitations. First, the emission inventory usually has a temporal lag of at least 2 to 3 years, as time is needed to aggregate information from different sources and format them into the emission inventories that are suitable for use in climate models. Second, the temporal resolution of the current emission inventory is usually on monthly to annual scale, which is not sufficient to characterize the daily or diurnal variation of emissions;

the aerosol impact on radiative transfer and the variation of cloud properties, however, is often strongly dependent on the time of the day [Wang et al., 2006]. Third, the spatial resolutions of the bottom-up emission inventories are usually limited by the availability of the ground-based observations, which often lack the spatial coverage for estimating emission in a uniformly fine resolution for regional modeling of aerosol transport. Finally, bottom-up emission inventories may miss important emission sources that are not well documented including emissions from wild fires, volcanic eruptions, and agricultural activities. All these limitations are amplified over the East Asia region because the economic growth in China is so rapid that information needed for bottom-up approach cannot be timely and reliably documented.

To complement information from bottom-up emissions, remote sensing is increasingly used to better quantify aerosol distributions. The satellite observations and/or products can provide information important for the bottom-up estimate of emissions. Examples include the fire products from MODIS, ASTER, and AVHRR sensors that are widely used for characterizing the biomass burning emissions [Borrego et al., 2008; van der Werf et al., 2006; 2010; Reid et al., 2009]. Alternatively, the satellite observed tracer abundance could be used to constrain bottom-up estimates of aerosol emissions through the inverse modeling; such method is referred to as a ‘top-down’ constraint. Although satellite-based aerosol retrievals have less precision than in situ measurements, studies have shown that they are able to quantify the atmospheric aerosol loading and temporal variations with good agreement and expected accuracy to the ground-based observations [Levy et al., 2010; Remer et al., 2005]. Furthermore, the satellite-based aerosol data, in contrast to the ground-based ones, have much higher temporal resolution across the globe. For instance, the MODIS sensor, aboard on NASA’s both Terra and Aqua satellites, has a surface footprint size of about 1 km at nadir and needs only 1 to 2 days to achieve global coverage. In addition, the joint retrieval of aerosols from diverse satellite sensors enhances the accuracy of satellite aerosol

products [Sinyuk et al., 2008], the potential of which have also been shown in the air quality monitoring [Liu et al., 2005; Wang et al., 2010].

Different top-down techniques have been developed to optimally estimates the emissions from satellite observations, which include but are not limited to the following:

- (a) the use of a scaling factor that is the ratio of observed tracer abundances to the CTM simulated counterparts [e.g. Lee et al., 2011; Martin et al., 2003; Wang et al., 2006];
- (b) the use of the local sensitivity of change of tracer concentration to the change of emission [e.g. Lamsal et al., 2011; Walker et al., 2010];
- (c) the analytical Bayesian inversion method [e.g. Heald et al., 2004];
- (d) the adjoint of CTM [e.g. Müller and Stavrakou, 2005; Henze et al., 2007; 2009; Dubovik et al., 2008; Kopacz et al., 2009; 2010; Wang et al., 2012].

The first two methods are similar; both assume a linear relationship between model simulated aerosol abundances and emissions. The analytical method is exact but computationally expensive and thus can only constrain emission in the domain-wise or over coarse spatial resolution [Kopacz et al., 2009]. In contrast to the first three approaches, the adjoint approach is designed for exploiting the high-density of observations to constrain emission with high resolution [Kopacz et al., 2009], as it is able to efficiently calculate gradients of the overall mismatch between observations and model estimates with respect to large sets of parameters (i.e., emissions resolved at each grid box) [Henze et al., 2007].

Several studies have successfully analyzed sources of traces gases using the top-down methods, including CO sources from MOPITT sensor over the Asia [Heald et al., 2004; Kopacz et al., 2009;] and over the globe [e.g. Stavrakou and Müller, 2006; Kopacz et al. 2010], CO₂ surface flux from the TES sensor [Nassar et al., 2011], NO_x emissions

from space-based column NO_2 by several satellite sensors [Lamsal et al., 2011; Lin et al., 2010; Martin et al., 2003; Müller and Stavrou, 2005], and SO_2 from SCIAMACHY and OMI sensors [Lee et al., 2011], etc. However, not all emissions of trace gases can be fully constrained with their satellite-based counterpart products, because some trace gases (e.g. SO_2) can react with other gases (e.g. NH_3), to form either liquid or solid aerosols (e.g. $(\text{NH}_4)_2\text{SO}_4$). As a result, using measurements of trace gases alone can only provide partial constraints on the emission of the corresponding trace gases.

1.1.2 Satellite Observations of Aerosol

Table 1.1: List of satellite sensors with measurement specifications relevant for operation retrieval of aerosol properties.

Sensor	Measurement Specification	Retrieved Aerosol Property	References
AVHRR ^a	15 bands at single view angle	AOD	Dubuisson et al [2009]
CALIOP	Layer backscattering and depolarization ratio	AOD profile	Winker et al [2010]
MERIS	15 bands at single view angle	AOD	Dubuisson et al [2009]

1.2 Main Goals of This Work

Based on the preceding discussions, this work aims at improved estimates of global dust emissions through adjoint integration of AOD retrievals from multiple satellite platforms (MODIS and MISR) with a CTM (GEOS-Chem). The overall goal is to conduct the satellite-based global model estimates of atmospheric dust distribution, and thereby advance the understanding of the impacts of atmospheric mineral dust on climate change and air quality. To accomplish this goal, this work pursues the following specific objectives:

- Develop a top-down numerical inversion scheme for constraining global dust emissions with a combined use of multi-platform AOD products and CTM adjoint, which also includes the sensitivity and error budget analysis for the optimization.
- Apply the inversion scheme developed in step 1 for a one year (i.e. 2008) of dust emissions with level 3 quality-controlled MODIS DB and MISR AOD products.
- A long-term (from 2001 to 2010) analysis of dust emissions will follow, along with studies on the seasonal and inter-annual variability of dust emissions, loadings, and direct radiative effects.
- Wherever possible, ground-based and field data will be used to validate and analyze the uncertainties of the inversion results.

Although the adjoint optimization technique we use is similar to that in Dubovik et al. [2008] and Yumimoto et al. [2007], this study differs from the those previous studies in that: (a) Multi-platform AOD products utilized to optimize dust emissions can provide tremendous dust information in fine spatial and temporal scales; (b) This study uses the satellite AOD retrievals only over and near dust source regions where dust has been transported a short distance with minimal influence of precipitation and anthropogenic aerosols; (c) Optimization of the long-term dust emissions is conducted for every grid box as a function of time (e.g., on the weekly or month scale). Although the criteria for separation of a natural and anthropogenic dust source is not clear and sometime controversial in the literature [Denman et al., 2007], especially when considering the climatic feedback on dust emissions [Zhang et al., 2002], we believe that satellite-based optimization of global dust emissions in the last decade could improve our modeling of dust radiative forcing and potentially illuminate anthropogenic components of dust sources and loadings, currently estimated at

0-20% though values as large as 50% has been postulated [Ginoux et al., 2011; Tegen et al., 1996; 2004; Mahowald et al., 2004,].

1.3 Organization of This Dissertation

We describe the GEOS-Chem simulation of mineral dust in Chapter 2 with emphasizing the physical parameterization of dust sources, after which we present the implements for the AOD observation operator and the adjoint capacity of dust emission within the GEOS-Chem adjoint model in Chapter 3. In chapter 4, we present a case study on optimizing the dust emission estimates from the satellite (MODIS) radiances over the eastern Asia, in which we also attempt to simultaneously constrain the anthropogenic emissions of the SO_2 , NO_2 , NH_3 , and carbaceous aerosols together with the dust aerosols. In chapter 5, we optimize the dust source parameterization from multi-satellite AOD products, particularly in improving the the estimates of soil erodibility and wind friction threshold for sand saltation over the northern Africa. Finally, we summarize the dissertation and outlook future work in Chapter 6.

CHAPTER 2

TOP-DOWN INVERSION FRAMEWORK

Overview Mathematically, solving an inverse problem involves two types of development, i.e., the forward modeling and inverse modeling. This chapter presents how the physical process that mineral dust involved are quantitatively represented in a chemistry transport model, i.e., the GEOS-Chem model. These processes include the uplifting of dust from soil surface, the transport within the atmosphere, and deposition of dust to the surface.

2.1 Inversion Theory and Infrastructure

Let \mathbf{x} denote a state vector of n parameters to be constrained and \mathbf{y} an observation vector assembled by m measurements, and let \mathbf{F} indicate a forward model that describes the physics of the measurement process. Then, we can express the relationship between the observation vector and the state vector as

$$\mathbf{y} = \mathbf{F}(\mathbf{x}) + \boldsymbol{\epsilon}, \quad (2.1)$$

where $\boldsymbol{\epsilon}$ is an experimental error term that includes observation noise and forward modeling uncertainty.

For this work, the observation vector \mathbf{y} comprises measurements of aerosol loading, such as mass concentrations or optical depth, at any temporal and spatial scale. The components of the state vector \mathbf{x} could vary according to our inversion focus. For the inversion of aerosol

emission estimates (as in the Chapter 3), \mathbf{x} comprises the emission fluxes (or their scaling factors) of defined aerosol species within each grid cell of specified temporal resolution. In contrast, \mathbf{x} consists of dust emitting parameters (or their scaling factors) when we tend to constrain the dust emission parameterization (as in the Chapter 4). The forward model \mathbf{F} represents the GEOS-Chem that maps parameters from the state space to the observation space. The inversion of the state vector from these measurements is often an ill-posed problem due to non-linearity and limited sensitivity of these observed quantities to the constrained parameters. We need to combine additional constraints to make the problem amenable to inversion.

A priori information describes our knowledge of the state vector before measurements are applied. *A priori* constraint is commonly used to achieve a well-defined stable and physically reasonable solution to an ill-posed problem. Usually, *a priori* knowledge comprises both a mean state \mathbf{x}_a and its error ϵ_a :

$$\mathbf{x} = \mathbf{x}_a + \epsilon_a \quad (2.2)$$

Under assumption of Gaussian-distributed errors, the Maximum A Posteriori solution of equations (2.1) and (2.2) according to the Bayesian approach corresponds to the state vector that minimizes the quadratic cost function [Rodgers, 2000]:

$$J(\mathbf{x}) = \frac{1}{2} [\mathbf{F}(\mathbf{x}) - \mathbf{y}]^T \mathbf{S}_y^{-1} [\mathbf{F}(\mathbf{x}) - \mathbf{y}] + \frac{1}{2} \gamma (\mathbf{x} - \mathbf{x}_a)^T \mathbf{S}_a^{-1} (\mathbf{x} - \mathbf{x}_a), \quad (2.3)$$

where T indicates the transpose operation, \mathbf{S}_y is the error covariance matrix of measurements, \mathbf{S}_a is the error covariance matrix of the *a priori*, and γ is the regularization parameter. These two terms on the right side of equation (2.3) represent the total squared fitting error incurred owing to departures of model predictions from the observations and the penalty error

incurred owing to depatures of the estimates from the *a priori*, respectively. Thus, the minimization of $J(\mathbf{x})$ achieves the objectives of improving the agreement between the model and the measurements while ensuring that the solution remains within a reasonable range and degree of smoothness.

The regularization parameter γ in the calculation of $J(\mathbf{x})$ acts weights to balance the fitting error and the penalty error. Clearly, a good assignment of γ is of crucial importance for the statistically optimal solution. High values of γ can lead to over-smoothing of the solution with little improvement to the fitting residuals, while low values minimize the error term at the cost of greatly increasing the penalty term. Optimal values of γ can be identified at the corner of the so-called L-curve [[Hansen, 1998](#)].

In principle, solving this inverse problem is tantamount to a pure mathematical minimization procedure. The minimization of $J(\mathbf{x})$ is performed with an iterative quasi-Newton optimization approach using the L-BFGS-B algorithm [[Byrd et al., 1995](#); [Zhu et al., 1994](#)], which offers bounded minimization to ensure the solution stays within a physically reasonable range. The L-BFGS-B algorithm requires knowledge of \mathbf{x} and $J(\mathbf{x})$, as well as the gradient of $J(\mathbf{x})$ with respect to \mathbf{x} , $\Delta_{\mathbf{x}}J$. By linearizing the forward model $F(\mathbf{x})$, we can determine $\Delta_{\mathbf{x}}J$ by

$$\Delta_{\mathbf{x}}J = \mathbf{K}^T \mathbf{S}_y^{-1} [\mathbf{F}(\mathbf{x}) - \mathbf{y}] + \gamma \mathbf{S}_a^{-1} (\mathbf{x} - \mathbf{x}_a), \quad (2.4)$$

where \mathbf{K} is the Jacobian matrix of $\mathbf{F}(\mathbf{x})$ with respect to \mathbf{x} , which is computed analytically by adjoint method in the GEOS-Chem adjoint. At each iteration, improved estimates of the state vector are implemented and the forward simulation is recalculated. The convergence criterion to determine the optimal solution is the smallness of the $J(\mathbf{x})$ reduction and the norm of $\Delta_{\mathbf{x}}J$. The iteration stops when the reduction of $J(\mathbf{x})$ is less than 1% within five continuous iterations. Then, the optimal solutions are identified corresponding to the smallest norm of $\Delta_{\mathbf{x}}J$ among these five last iterations.

2.2 GEOS-Chem Forward Modeling

The GEOS-Chem chemistry transport model is used to simulate the ambient concentrations of atmospheric aerosols.

The GEOS-Chem aerosol simulation was based on the GOCART model [Chin et al., 2002], particularly for wet scavenging, with updates described by Park et al. [2004].

Particularly for the interest of this study

2.2.1 Anthropogenic aerosol emissions

2.2.2 Dust emissions

The dust emission, aerolian wind erosion that results in production of mineral aerosols from soil grains, involves complex and nonlinear processes that are governed by the meteorology as well as by the state and properties of the land surfaces. Laboratory [Iversen and White, 1982] and field [Shao et al., 1996; Zender et al., 2003] wind tunnel studies suggested that dust is primarily injected into the atmosphere during the sandblasting caused by the saltation bombardment [Alfaro and Gomes, 2001; Grini et al., 2002]. The clay- and silt-sized soil particles have strong inter-cohesive force... The saltation of sand-sized particles ... requires least threshold of wind speed...

The most important factors include wind friction velocity and its threshold for saltation, vegetation cover, soil minerology, and surface soil moisture.

In this study, the physical parameterization of dust emission is taken from a Dust Entrainment and Deposition (DEAD) model developed by Zender et al [2003a]. The DEAD scheme calculates the wind friction threshold (u_{*t}) as a function of the Reynolds number following Iversen and White [1982] and Marticorena and Bergametti [1995]. Three processes are also considered to modify the u_{*t} : the drag partitioning owing to the momentum captured

by nonerodible roughness elements, the Owen effect, and moisture inhibition. The horizontal saltation flux (Q_s) that is defined as the vertical integral of the stream-wise soil flux density is calculated following the theory of White [1979]:

$$Q_s(u_*, u_{*t}) = \frac{c_s \rho}{g} u_*^3 \left(1 - \frac{u_{*t}}{u_*}\right) \left(1 + \frac{u_{*t}}{u_*}\right)^2, \quad (2.5)$$

where, $c_s = 2.61$, ρ is the air density at surface level, and u_* is the wind friction velocity. Thus, it assumes the saltation flux is quasi-linearly the u_*^3 when u_* exceeds the u_{*t} . It also neglect the dependence of total Q_s on the soil size.

the total vertical mass flux of dust into transport bin j is

$$E_{d,j} = \begin{cases} T_0 A_m S \alpha Q_s \sum_{i=1}^3 M_{i,j} & \text{if } u_* \geq u_{*t}, \\ 0 & \text{if } u_* < u_{*t}, \end{cases} \quad (2.6)$$

where, T_0 is a tuning factor chosen to adjust the global amount, A_m is the fraction of bare soil exposed in a model grid cell, S is called "erodibility" or "preferential source function", α is the sandblasting mass efficiency factor which depends on the mass fraction of clay particles in the parent soil, and $M_{i,j}$ indicates the mass fraction of i th source mode carried into the j th transport mode.

2.3 GEOS-Chem Adjoint Modeling

The adjoint of the GEOS-Chem model was developed specifically for inverse modeling of aerosol (or their precursors) and gas emissions [Henze *et al.*, 2007, 2009], and it is continuously improved and maintained by the GEOS-Chem Adjoint and Data Assimilation Working Group and its users (<http://wiki.seas.harvard.edu/geos-chem/index>).

[php/GEOS-Chem_Adjoint](#)). The strength of the adjoint model is its ability to efficiently calculate model sensitivities with respect to large sets of model parameters, such as aerosol emissions at each grid box. These sensitivities can serve as the gradients needed for inverse modeling of aerosol emissions. Recent studies have used the GEOS-Chem adjoint with satellite observations to constrain sources of species such as CO [*Kopacz et al.*, 2009, 2010; *Jiang et al.*, 2011], CH₄ [*Wecht et al.*, 2012], and O₃ [*Parrington et al.*, 2012] to diagnose source regions for long-range transport [*Henze et al.*, 2009; *Kopacz et al.*, 2011], and to provide guidance on future geostationary observations of surface air quality [*Zoogman et al.*, 2011].

CHAPTER 3

OPTIMIZING SPECIES-SPECIFIED AEROSOL EMISSIONS

3.1 Introduction

In this chapter, we present a new attempt for the top-down estimate of aerosol emissions through integration of the satellite observation of reflectance and GEOS-Chem Adjoint model. The technique is applied to improve estimates of mineral dust and anthropogenic SO_2 , NH_3 , NO_x , BC and OC emissions over China for April 2008, during which ground-based PM_{10} (particulate matter with aerodynamic diameter of $10\text{ }\mu\text{m}$ or less) data is available from a joint China-U.S. dust field experiment [Huang et al., 2010]. This paper differs from the past work in that: (i) satellite reflectance (in essence radiance) is used to constrain the emission estimates of aerosol particle and precursors, which eliminates the discrepancy of aerosol optical properties between model simulated and satellite retrieved AOD; (ii) we use a suite of aerosol and gas measurements from satellite sensors and ground-based instruments to independently evaluate our results, and test our hypothesis that temporal variation of AOD at different locations, as characterized by satellite observations, can be a strong constraint for species-specific source estimates if they are combined with the model-based knowledge of the dominant aerosol sources and the source-receptor relationship at corresponding locations; and (iii) combination of (i) and (ii) will provide the basis and a necessary step forward for future research to simultaneously use both gas and AOD measurements to constrain speciated aerosol emissions.

We describe the top-down inversion scheme and its key components (i.e., GEOS-Chem forward model and its adjoint, and observational constraints) in Section 2. The top-down constraints on aerosol emissions over China for the period of April 2008 are presented in Section 3, and evaluated in Section 4. Interpretation and implications of the results are discussed in Section 5, and Section 6 summaries this study. [needs updates!!!!]

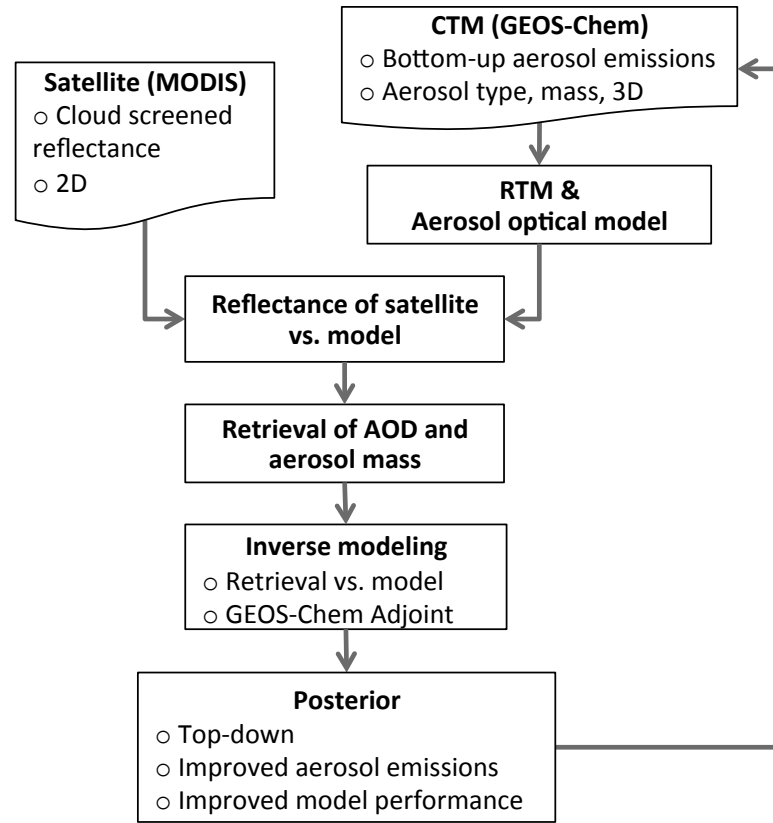


Figure 3.1: Flowchart of the proposed top-down inversion framework.

As shown in Figure 3.1, the top-down inversion approach in this study integrates the MODIS radiance/reflectance with the GEOS-Chem (section 2.1) and its adjoint model (section 2.2) to optimize aerosol emissions. First, similar to Wang et al. [2010], we retrieve the atmospheric aerosol mass and AOD through fitting the calculated radiance based on GEOS-Chem aerosol composition and single optical properties to the MODIS cloud-free

radiances (section 2.3). Second, the retrieved AOD (hereafter retrieved MODIS AOD) from the first step is used as an observational constraint to optimize the aerosol emissions by inverting the GEOS-Chem chemical transport model (section 2.4). The approach aims to improve aerosol emission estimates that ultimately will yield better agreement between model simulated and satellite-observed reflectances. Since the aerosol single scattering properties are exactly the same between the retrieval algorithm and GEOS-Chem (as done in the first step), the top-down inversion scheme essentially uses the MODIS radiances (in the form of retrieved AOD) to scale the GEOS-Chem aerosol mass, which in turn are used to optimally adjust the aerosol emissions. The approach here is first demonstrated through a pseudo-observation experiment (Section 2.5) before it is applied to real observations (Section 3).

3.2 Constraints from Satellite Radiances

The observational constraints in this study are MODIS reflectances from both Terra and Aqua satellites, from which four-dimensional mass concentrations of six aerosol species (namely, SO_4 , NO_3 , NH_4 , BC, OC, and dust) have been derived with the GEOS-Chem model using the retrieval algorithm presented by Wang et al. [2010]. Key to this algorithm are: (a) a database of time-dependent local 0.65 and 2.1 μm surface reflectance ratio that are derived from samples of the MODIS dark-pixel reflectance data in low AOD conditions (i.e. dynamic lower envelope method), (b) an assumption that the simulated CTM aerosol is unbiased in composition and vertical distribution shape but possibly largely biased in total mass or optical depth, and (c) a linearized radiative transfer model (VLIDORT [Spurr, 2006]) that computes the top-of-atmosphere (TOA) reflectance and its Jacobian sensitivity to the column AOD using the GEOS-Chem single aerosol optical properties and the solar-earth-sensor geometries of the coincident MODIS scene. With above (a), (b), and (c), Wang

et al. [2010] retrieved two unknowns (AOD at $0.65\ \mu\text{m}$ and surface reflectance at $2.13\ \mu\text{m}$) from two MODIS observed quantities (0.65 and $2.13\ \mu\text{m}$ TOA reflectance) by seeking the minimum differences between GEOS-Chem and MODIS reflectance. Based on (b), mass concentrations of individual aerosol species at each MODIS overpassed grid cell are updated by applying the AOD scaling factors (ratios of retrieved AOD to GEOS-Chem AOD at $0.65\ \mu\text{m}$) and are used as observational constraints for optimizing aerosol emissions. According to the evaluation of the retrieved AOD against AERONET AOD [Wang et al., 2010], we found the uncertainty is generally less than 20%, which we subsequently use to quantify the observation error in the inverse modeling optimization.

GEOS-Chem simulated aerosol composition over Asia is shown by multiple studies to have large underestimation in BC, and equivalent or larger underestimation of OC mass and overestimation of sulfate aerosol mass [Heald et al., 2005; Fu et al., 2012], which suggests that the mass fraction of highly absorbing (BC) and highly scattering (OC and sulfate) fine mode aerosols may have far less biases (as compared to the relative bias in OC mass only). Consequently, no significant biases are assumed for: (a) the GEOS-Chem simulated fraction of coarse mode (dust) aerosol mass, and (b) the GEOS-Chem simulated aerosol single scattering albedo. While (b) is important to ensure an unbiased retrieval of AOD, (a) supports that the GEOS-Chem simulated dust AOD fraction is likely unbiased, both of which support the use of AOD scale factors derived from MODIS for constraining emission of coarse-mode dust and fine-mode aerosols. Admittedly, any model bias in modeled AOT fraction for each individual species can lead to a corresponding bias (of the same sign) in the adjoint modeling results for individual emission. Quantification of such bias is not possible for the present study owing to the lack of aerosol composition data in China.

3.3 Inversion Strategies

3.3.1 Selection of emissions for optimization

The inversion scheme and the MODIS-based constraints, as described in the last three sections, are combined to constrain the aerosol emissions over the Eastern Asia for the period of April 2008. The modeled emission parameters that most significantly influence the discrepancy between simulation and observations are selected and spatially constrained. Specifically, those model parameters (or control parameters) represent six emitted tracers, as listed in Table 2, which include emissions of SO_2 , NH_3 , and NO_x , BC, and OC from anthropogenic sources, and mineral dust. Bottom-up inventories (and an online mobilization scheme for dust) are used as *a priori* estimates, corresponding magnitudes and geographic distributions of which are shown in Table 2 and Figure 3.5, respectively. The temporal extent of the optimization window is selected to be reconcilable with the temporal variability of the bottom-up emission. We set optimization window of a month for those trace gases and carbonaceous emission tracers; while dust emission tracers are constrained daily in a separate optimization run following approach by Wang et al., [2012]. Both optimizations assimilate hourly observations during the adjoint simulation.

The 4D-Var technique in the optimization requires background error covariance statistics for each control parameter. We specify the priori error for those emission tracers based on characterized spatial and temporal averaged uncertainties for those inventories [Zhang et al., 2009; Bond et al., 2007; Zender et al., 2003] but with larger values to reflect the possibly large local aerosol emission uncertainties in the bottom-up inventories. The uncertainty for SO_2 emission estimate is believed to be smaller than those for NH_3 and NO_x , while uncertainties of other tracers could be even larger [Textor et al., 2006; Zhang et al., 2009]. Therefore, we set relative error of 50% for SO_2 , 100% for NH_3 and NO_x , 200% for BC,

OC, and dust sources. Lacking information to fully construct a physically representative prior error covariance matrix, a regularization parameter γ is introduced in the cost function to balance the contribution of model error and source error, with a value (here $\gamma = 1000$) selected using the L-curve technique [Hansen, 1998]. Moreover, in order to test the impact of those specified uncertainties on the optimization, we run a case with an arbitrary prior error of 100% for all emission tracers, and present the results in Table 3.

3.3.2 Sensitivity test with pseudo AOD observations

We first conduct a pseudo experiment to assess: (1) the concept that temporal variations and geophysical location of AOD, when interpreted with GEOS-Chem model, can yield information about change regarding aerosol composition and emissions, and (2) the sensitivity of the inversion results to the assumption that GEOS-Chem simulated relative composition or single scattering albedo of aerosol is unbiased. The experiment has three steps: (a) GEOS-Chem simulation with standard bottom-up EIs are first conducted to obtain prior aerosol composition and $0.65 \mu\text{m}$ AOD for the period from April 5 to 11 of 2008; (b) Pseudo-observations of AOD are created by perturbing the following emissions (relative to bottom-up EIs) in GEOS-Chem: +20% for SO_2 , NH_3 , and NO_x , -40% for dust, and zero for BC and OC (Table 1); (c) These pseudo-observations of AOD in the dark surface region (red box in Figure 2a), twice per day, respectively at the Terra and Aqua overpass daytime, are subsequently used as truth to constrain emissions using the GEOS-Chem adjoint-based inversion.

The degree to which the inversion can correct for species-specific errors in the emissions is assessed in these sensitivity tests by comparing the optimized aerosol emissions from (c) can then be evaluated against the truth, or the perturbed emissions in (b). Figure 3.1 shows the distribution of relative changes in posterior emissions from the 6th iteration with

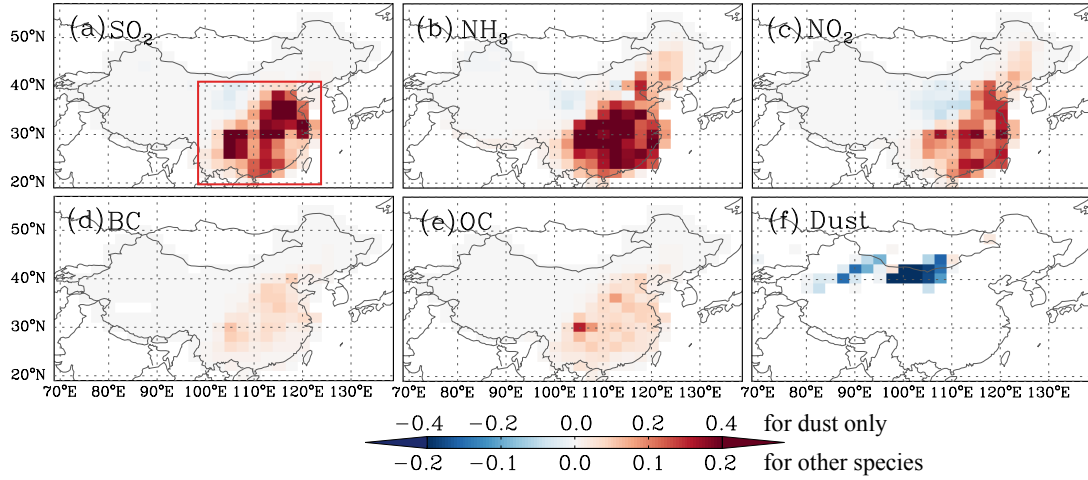


Figure 3.2: Relative changes in posterior aerosol emissions from *a priori* in the pseudo-observation experiment. Six panels are respectively for anthropogenic emissions of SO_2 , NH_3 , NO_x , BC, and OC, and mineral dust from both natural and anthropogenic sources. The red box in panel (a) indicates the region where AOD observations are selected.

respect to the prior bottom-up emissions for each species; the overall changes over the China are shown in Table 3.1. By the 6th iteration, the cost function reduced by 50%; further iterations yielded negligible additional decreases. The posterior emissions for SO_2 and NH_3 , which increased by 14% from the prior, are close to the “truth” (20%). NO_x emissions were increased by 8%, a smaller change than SO_2 and NH_3 . Dust emissions reduced by 26% percent in the inversion, approaching the true values of -40%. BC and OC emissions were increased by 2% and 3%, which are close to the truth of 0.

Overall, this sensitivity study demonstrates that the inversion is capable of resolving the sign, spatial distribution, and the bulk of the true perturbations for the emissions of each species. Meanwhile, we also note that the adjoint inversion could transfer (somewhat marginal) errors from one tracer to another, such as increases in BC and OC emission as a result of significant underestimations in the prior SO_2 , NH_3 , and NO_x emissions, reflecting errors due to assumptions related to unbiased GEOS-Chem aerosol composition. We can also assume that similar aliasing would occur in attempts to distinguish the impacts of co-

Table 3.1: Prior, posterior, and perturbed aerosol emissions over China in the pseudo experiment.

Tracer	E_{prior} (Gg/Month)	$E_{\text{posterior}}$ (Gg/Month)	$E_{\text{posterior}}/E_{\text{prior}}$ (%)	$E_{\text{perturbed}}/E_{\text{prior}}$ (%)
SO ₂	520.8	592.0	113.7	120
NH ₃	219.3	249.2	113.7	120
NO _x	338.8	365.3	107.8	120
BC	23.3	23.8	102.3	100
OC	39.7	41.1	103.4	100
Dust	2301	1697	73.7	60

located precursor emissions of scattering particles (e.g., SO₂ and NO_x from power plants), although additional tests would be necessary to assess whether or not differences in the timescales (and thus transported length scales) over which these emissions impact AOD would allow their sources to be separated. Long-range transport of dust appears to have less influence on the inversion because: (a) except dust, there are little (other) emissions in dust source regions; (b) a sudden increase of AOD in downwind regions can be interpreted by GEOS-Chem due to the dust transport, and this increase can be used by GEOS-Chem adjoint as constraint to optimize the dust emission.

3.4 Inversion Results

With the feasibility of the approach demonstrated in Section 2, we apply the approach to MODIS radiance data in April 2008. The emissions that result from each iteration during the optimization enable GEOS-Chem to produce a different set of AOD values that converge to the observational constraints. Figure 3.3c shows the geographic distribution of GEOS-Chem AOD at 0.65 μm , simulated with prior aerosol emissions, averaged coincidentally with retrieved daily MODIS AOD (Figure 3.3c) during April 2008. While the prior model simulation captures the overall spatial pattern of AOD with larger values over eastern

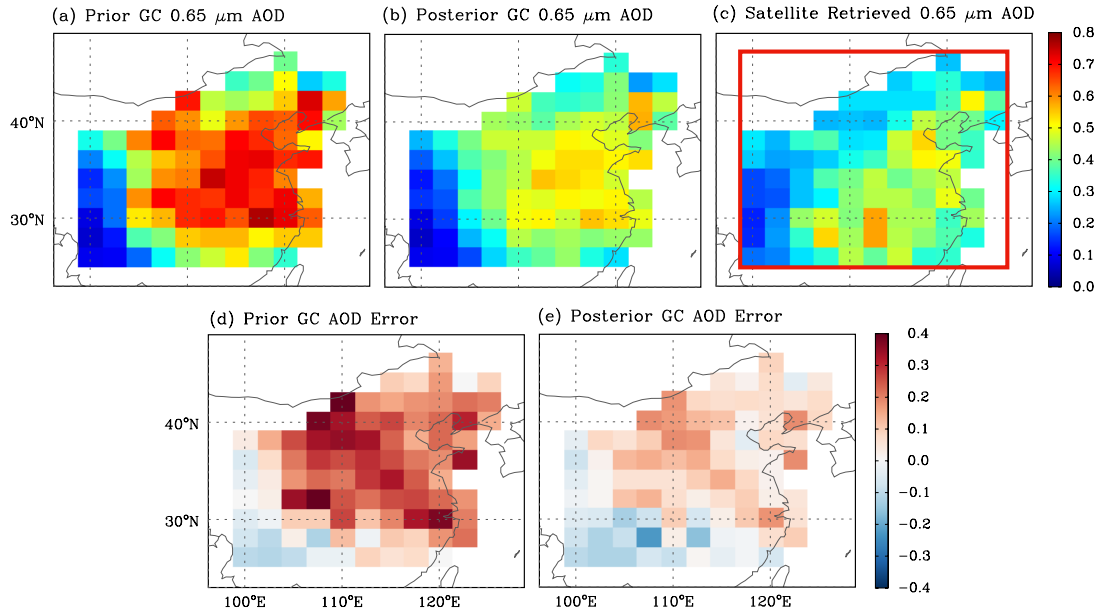


Figure 3.3: Comparison of the prior (a) and posterior (b) GEOS-Chem (GC) simulation of $0.65 \mu\text{m}$ AOD with the AOD at the same wavelength retrieved from MODIS reflectance using GEOS-Chem aerosol optical properties (c) averaged for the period of April 2008. Satellite retrievals with 10 km by 10 km at nadir are aggregated to GEOS-Chem grid cells; and the model AOD are sampled coincidentally with those retrievals. Panel (d) and (e) respectively show the difference of prior and posterior simulated from the satellite retrieved AODs. The red box in panel (c) indicates the region where AOD observations are selected.

China, it has a slight underestimation over the southwestern China but an overwhelming overestimation elsewhere, when compared to the retrieved AOD from MODIS radiance (Figure 3.3d). The optimization is expected to adjust aerosol emissions to reduce those differences. Following the experiment design described in section 3.3.1, we find that after 6 iterations of the GEOS-Chem forward and adjoint runs, the cost function is reduced by about 60%, and further iterations yield negligible reductions in the cost function. Therefore, the aerosol emissions adjusted in iteration 6 are selected as the final optimal results. As shown in Figure 3.3b and 3.3e, the posterior GEOS-Chem AOD that are simulated with the optimized aerosol emissions are in much better agreement with their counterparts retrieved from MODIS reflectance, which is also reflected by the cost function reduction and confirms

the effectiveness of the adjustment in top-down emissions.

The convergence of the model simulation to the MODIS AOD retrievals is also indicated in the AOD daily variability. Figure 3.4a shows the daily variations of the AOD spatially averaged for available MODIS retrievals (purple) over the eastern China areas within the red box in Figure 3.3c, and the coincidental GEOS-Chem simulation prior and posterior to the aerosol emission optimization (orange and green, respectively). The prior model produce overestimated AODs for most days during the month. After top-down adjustments to the aerosol emissions, such overestimation of the AOD is reduced in total over the course of the month. As shown in Figure 3.4b, the real changes of the modeled daily AOD during the optimization (green bars), or equivalently, the differences of the posterior from the prior are consistent with the expected changes, i.e., the differences of the MODIS retrievals from the prior model simulation. It is noted that the posterior AODs has larger departure from the observation than the prior on a few days. This reflects that monthly-scaled emissions are not perfectly capturing the daily variation of emission.

Emissions of SO_2 , NH_3 , NO_x , BC, and OC from anthropogenic sources are optimized monthly and rescaled over each individual 2° by 2.5° grid cell of China for the month of April 2008. The prior and posterior (optimized) emissions of those tracers are respectively shown in left and middle columns of Figure 3.5, in which the relative changes of those emissions in the optimization are also included in the right column. Overall, the optimization yields an overwhelming reduction for all emission tracers, even though some local increases are found. As expected, such adjustment in the constrained aerosol emissions is consistent with the changes in GEOS-Chem AOD before and after optimization, as aerosol loadings usually positively respond to the aerosol emissions. Quantitatively, anthropogenic emissions over China continent for the study period are changed by -33.5% for SO_2 from 1.302 to 0.866 Tg, -34.5% for NH_3 from 1.096 to 0.718 Tg, -18.8% for NO_x from 1.694 to 1.375 Tg, -9.1% for BC from 0.11 to 0.10 Tg, and -15.0% for OC from 0.205 to 0.175 Tg (Table 2). The

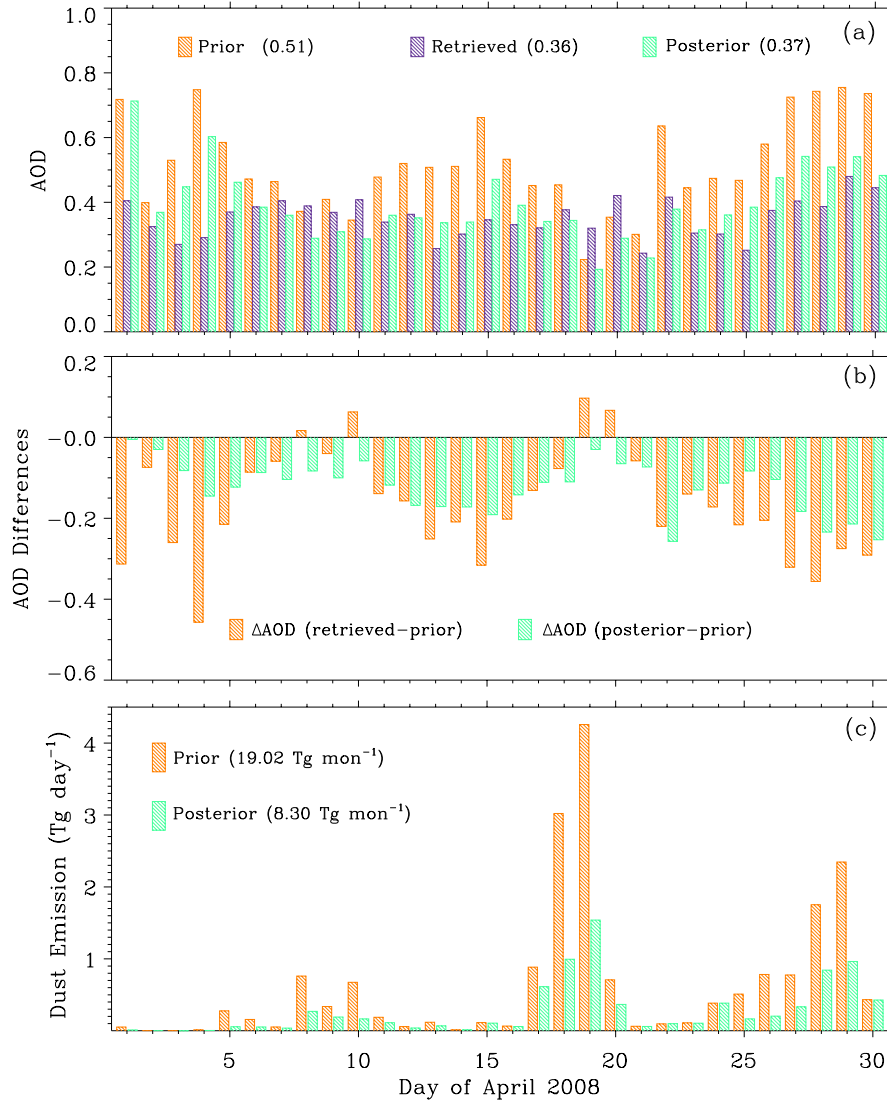


Figure 3.4: (a) Time series of the spatially averaged daily MODIS AOD retrievals (purple) for April 2008 over the Eastern China, compared by the prior (orange) and posterior (green) spatial averaged daily GEOS-Chem AOD that are sampled in the MODIS AOD temporal-spatial space. (b) Time series of the expected daily AOD adjustments (orange) that are the differences between MODIS AOD and the prior GEOS-Chem AOD and their real adjustments (green) that are the differences of posterior from prior GEOS-Chem AOD. (c) Time series of the prior (orange) and posterior (green) daily dust emissions over China for April 2008.

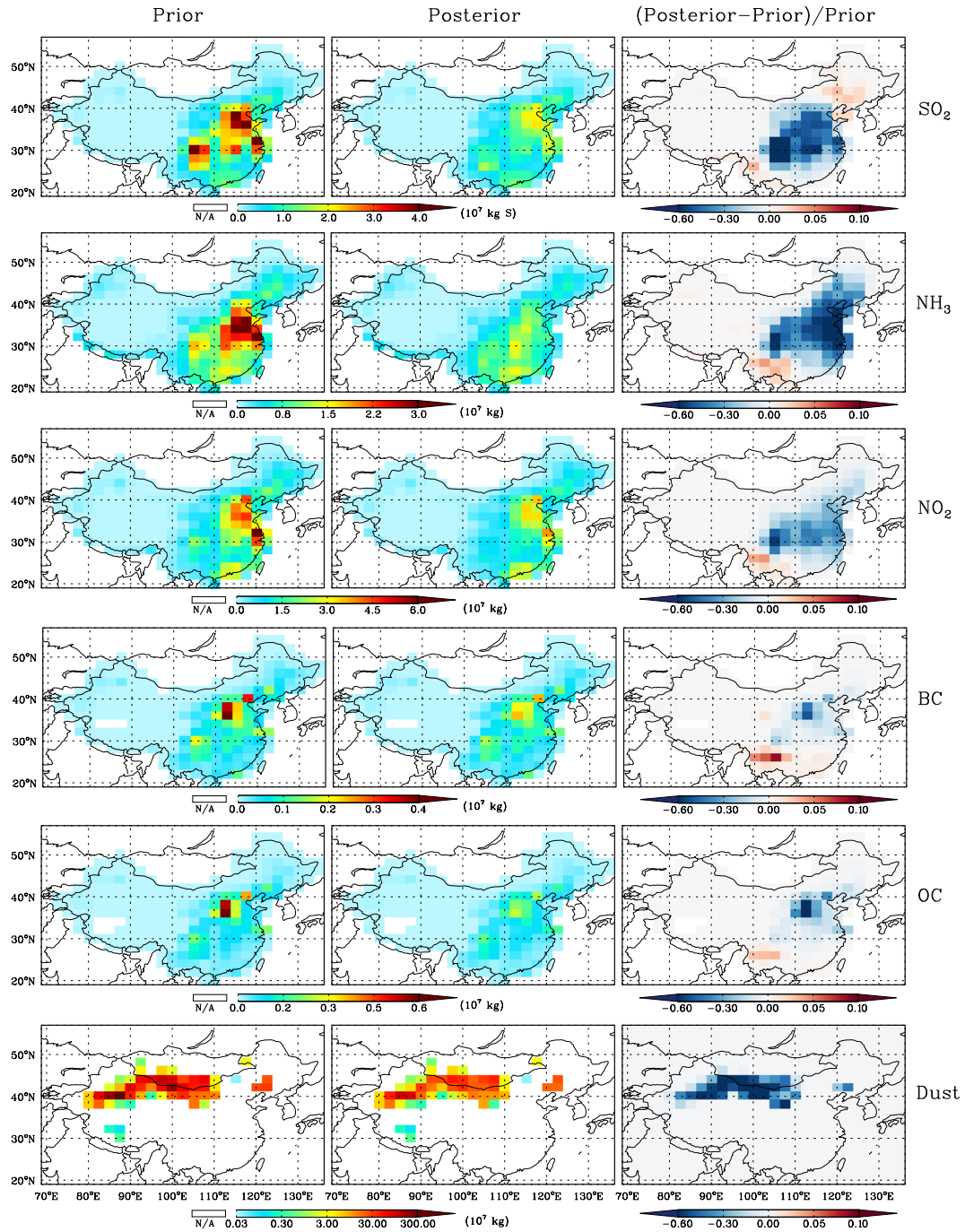


Figure 3.5: The prior (or bottom-up based, left column), optimized (or top-down constrained, middle column) aerosol emissions over China for the period of April 2008, and their relative differences (right column). Six rows from top to bottom are respectively for anthropogenic emissions of SO_2 , NH_3 , ceNO_x , BC, and OC, and mineral dust from both natural and anthropogenic sources.

largest reduction occurs sharply in the central regions of the Eastern China, corresponding to the region where the largest AOD are adjusted to the MODIS retrievals. Small increases of emitted anthropogenic sources of gases and carbonaceous particles are found over the southwestern China, which can be explained as the response for the underestimation of AOD in the model simulation over these regions (Figure 3.3a, d).

The mineral dust emissions from both anthropogenic and natural sources are optimized daily. The adjoint has no leverage to increase the dust emissions over grid cells having zero dust emission in the priori estimate identified by the modified DEAD scheme. Thus, the posteriori dust source region remains un-shifted as shown in Figure 3.5 (bottom panels), which is reasonable because the expansion or shrinkage of desert regions is unlikely to extend beyond the grid size (2° by 2.5°) of this study [Zender *et al.*, 2003; Fairlie *et al.*, 2007]. The total amount of the optimized dust emissions for April 2008 over China is 8.3 Tg, reduced by 56.4% from the modified DEAD module simulation of 19.02 Tg. Such reduction indicates an overestimation in the prior emissions of dust, especially over Gobi deserts that are located in the Northwestern China and the southern Mongolia. Wang *et al.* [2012] presented a similar result, but only for a dust event that occurred in the later portion of our study time period. Figure 3.4c illustrates the time series of the prior and optimized daily total dust emission. Two sharp peaks of the dust emissions indicate the occurrences of strong dust storms after April 15. Such large temporal variation in the daily scale requires the optimization of dust emission on the daily basis.

An additional case with specified error of 100% for all the anthropogenic emission tracers is conducted to examine the sensitivity of those specified error to the optimization. Table 3 shows the relative change in optimized emissions for two different scenarios. Less than 0.5% difference in the optimized emissions is found, which means the uncertainty in a priori emission could have much smaller impact on the optimization than the observational constraints.

3.5 Results Evaluations

Because direct measurements of the aerosol emissions are few over China, we assess the optimized sources by comparing the GEOS-Chem posterior simulated aerosol mass concentrations and AOD with the independent observations from various sources. The evaluation datasets include: (1) AERONET AOD observations [Holben et al., 1998] over nine sites; (2) Level 3 MISR daily AOD products [Kahn et al., 2005]; (3) Level 3 SO₂ [Krotkov et al., 2006; Lee et al., 2009] and Level 2 NO₂ [Bucsela et al., 2006] retrievals from the Ozone Monitoring Instrument (OMI); (4) surface mass concentration of sulfate-nitrate-ammonium (SNA) aerosol particles over Qingdao, China; and (5) surface PM₁₀ over two sites close to dust source region [Ge et al., 2010].

3.5.1 Comparison with AERONET AOD

We first evaluate the prior and posteriori GEOS-Chem 0.55 μm AOD against the AERONET AOD at 0.55 μm that are interpolated from AODs at 0.44 and 0.67 μm based on the Angstrom exponent. Three-hour averaged values of available AERONET AOD, centered by the model output time are used to compare with the model AOD over the grid cells locating the AERONET sites. The scatterplots shown in Figure 3.6 are the comparisons for nine stations over China, South Korea, and Japan representing different aerosol types. The first three stations, i.e., (a) Zhangye, (b) SACOL, and (c) Jingtai, which are located over rural regions in the south boundary of Gobi deserts and have little influence from anthropogenic emissions, are representative sites for dust aerosol [Ge et al., 2010]. The next three sites, (d) Beijing, (e) Xinglong, and (f) Heifei, are located in anthropogenic source regions. The last three sites, (g) Noto, (h) Shirahama, and (i) Gwangju_K, are located over Japan and South Korea, the downwind regions of China emissions. Those last six stations are affected not

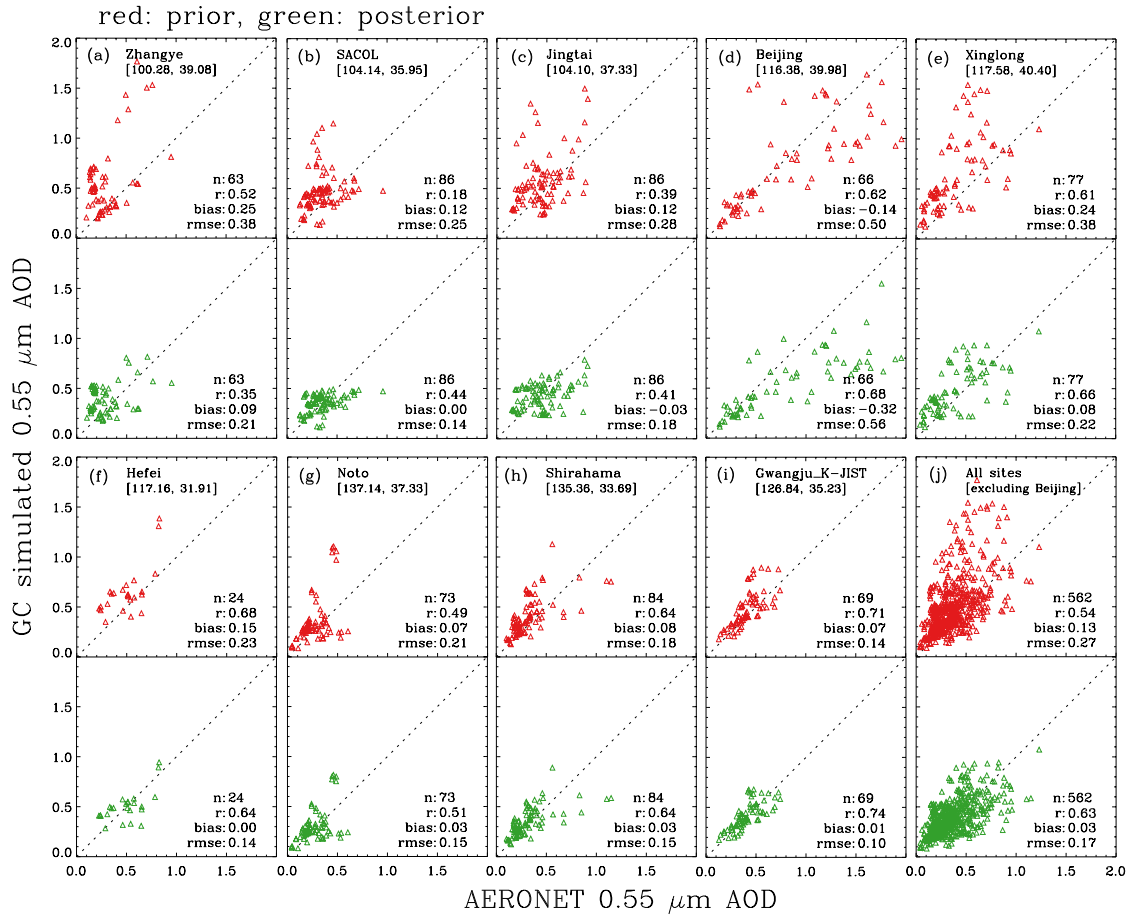


Figure 3.6: (a – i) Scatterplots of GEOS-Chem AOD versus AERONET AOD at $0.55 \mu\text{m}$ prior (red scatters) and posterior (green scatters) to the aerosol emission optimization over nine stations. AERONET AODs are 3-hour averages following the GEOS-Chem output frequency. (j) The overall comparison for eight AERONET sites excluding Beijing. Also shown are the number of valid sampled pairs (n), correlation coefficients (R), bias, and root-mean-square-error (rmse).

only by the local anthropogenic emissions but also by the long-range transported aerosols from the upwind regions. Indeed, those three categories of stations are respectively located in the upwind, central, and downwind of regions having the observational constraints.

The prior GEOS-Chem simulation (shown in the red scatter panels) overestimates the AERONET AOD for all the sites except Beijing. The low bias of model AOD at Beijing is likely owing to the model coarse resolution, which fails to resolve heavy local urban

pollution. The geographic area of urban Beijing is about 1300 km² (<http://en.wikipedia.org/wiki/Beijing>), less than 3% of the area of a GEOS-Chem grid cell. Thus, the local pollution signal is smeared in the model grid box. Moreover, Beijing and Xinglong are in the same model grid cell, but AERONET AOD over Xinglong is much smaller than that over Beijing site (as later shown as circles on the maps of Figure 3.7a-c). As Beijing site is difficult to represent in the GEOS-Chem at 2° by 2.5° resolution, we exclude Beijing site in our further analysis. GEOS-Chem AOD from the posterior aerosol emissions are in more agreement with the AERONET AOD (shown in the green scatter panels), as indicated by reduced bias and root-mean-square-error (rmse) over all the other sites and increased correlation coefficients (R) for most sites. The overall comparison (Figure 6j) shows the correlation coefficient increases from 0.54 to 0.63, and the bias (rmse) declines from 0.13 (0.27) to 0.03 (0.07).

3.5.2 Comparison with MISR AOD

We re-grid the Level 3 daily MISR 0.55 μm AOD from the 0.5° by 0.5° resolution to GEOS-Chem 2° by 2.5° grid cells and take monthly average for April 2008, the geographic distribution of which are shown in Figure 3.7c. High AOD values are found over the eastern China and the northwestern desert regions, which are associated to the anthropogenic pollution primarily from the industry and wind-blown mineral dust, respectively. The monthly sun-photometer AOD values at the same wavelength show good agreements with the MISR AOD over all the AERONET sites except Beijing where the significant local urban pollution exists.

The monthly averages of prior and posterior GEOS-Chem 0.55 μm AOD mapped in Figure 3.7a-b are sampled coincidentally to the MISR AOD. A comparison with the MISR AOD shows GEOS-Chem simulation with prior aerosol emissions overestimates AOD over

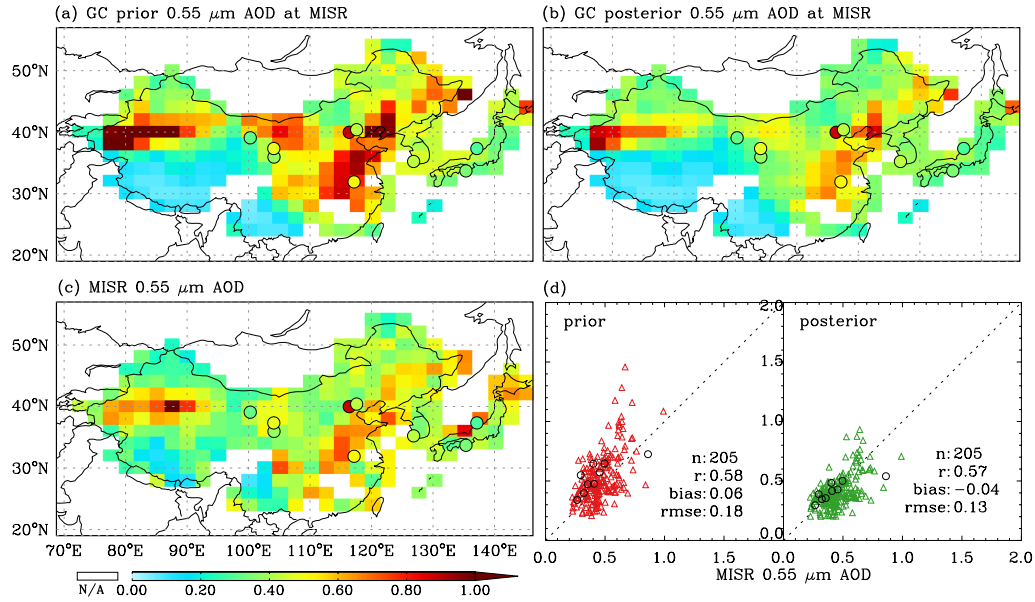


Figure 3.7: Comparison of the prior and posterior GEOS-Chem simulation of $0.55 \mu\text{m}$ AOD with the level 3 MISR $0.55 \mu\text{m}$ AOD for the period April 2008. (a) The prior GEOS-Chem $0.55 \mu\text{m}$ AOD that are sampled coincidentally with MISR AODs for the period of April 2008. Also overlaid circles are the monthly AOD averages at $0.55 \mu\text{m}$ observed from the nine AEORNET sites shown in Figure 3.6. (b) Same as (a) but for the monthly average of posterior GEOS-Chem AOD. (c) Monthly average of the Level 3 daily MISR $0.55 \mu\text{m}$ AOD. (d) Scatter plot the GEOS-Chem AOD versus the MISR AOD before (red scatters) and after optimization (green scatters), in which each point indicates an AOD pair over a model grid cell with value over 0.2. Also shown are the statistics including number of sampled pairs (n), correlation coefficient (R), bias and root-mean-square-error (rmse). Comparisons of the monthly GEOS-Chem AOD versus AERONET AOD are also included as the black circles; each circle indicates an AOD pair over an individual site.

both the desert and industrial regions. The posterior simulation is slightly more in agreement with MISR AOD. To facilitate the comparison of model with MISR AOD, we also include, as Figure 3.7d, the scatterplots of the AOD for each GEOS-Chem grid cell with values larger than 0.2 by considering the larger retrieval uncertainty in the low AOD conditions [Kahn et al., 2005]. While the correlation coefficients remain about the same, both absolute bias and rmse are reduced about 30%.

3.5.3 Comparisons with OMI Column SO₂ and NO₂

The improvement in the optimized aerosol emissions is also exhibited in the comparison of simulated trace gases to the satellite retrievals from OMI. The GEOS-Chem SO₂ simulations are assessed with OMI Level 3 daily products of planetary boundary layer (PBL) SO₂ column gridded with 0.25° by 0.25° resolution. We average the OMI SO₂ column retrievals into GEOS-Chem 2° by 2.5° grid cells and take the monthly average for comparison, which are shown in Figure 3.8c. Figure 3.8a and 3.8b show model prior and posterior SO₂ column that are coincidentally sampled with OMI retrievals. Figure 3.8d illustrates the quantitative analysis for OMI SO₂ retrievals larger than 1.0×10^{16} molec cm⁻². With the optimized emission estimates, the bias and RMSE are reduced from 0.81 and 0.61 to -0.28 and 0.38 (10^{16} molec cm⁻²), respectively, along with an increase of correlation coefficient from 0.68 to 0.73.

We evaluate the model simulation of NO₂ with OMI Level 2 products of NO₂ tropospheric column over 0.25° by 0.25° grid cells. Recent studies suggested that the uncertainty in OMI NO₂ tropospheric column retrievals is about 40% with an about 15% positive systematical bias [Boersma et al., 2008; Celarier et al., 2008]. Following Lin et al. [2010], we apply a factor of 0.85 to OMI NO₂ retrievals in our comparison to correct the bias. Figure 3.9 shows the comparison of GEOS-Chem NO₂ columns with re-gridded OMI NO₂ retrievals. Similarly, we also perform the quantitative analysis, as in Figure 3.9d, for OMI NO₂ column retrievals larger than 3.0×10^{15} molec cm⁻². While the correlation coefficient remains about the same, the bias (RMSE) is reduced from 1.50 (1.65) to 0.03 (1.51) (units: 10^{15} molec cm⁻²) after constraining aerosol emissions.

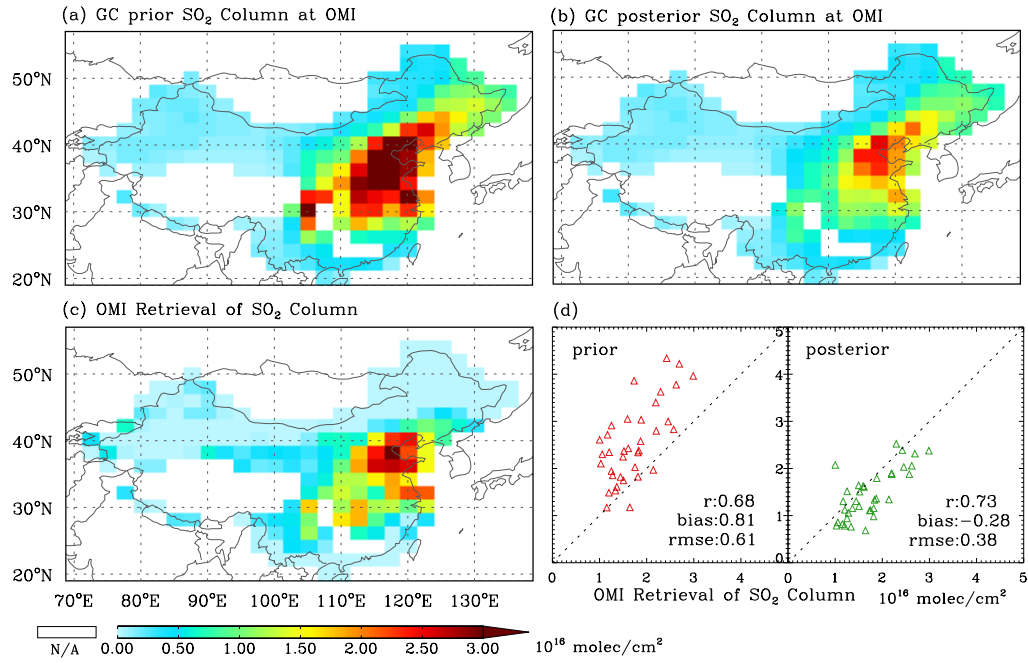


Figure 3.8: Same as figure 3.7 but for comparison of the GEOS-Chem SO₂ simulation with OMI column SO₂ retrievals for the period of April 2008. The OMI planetary boundary layer (PBL) column SO₂ from the Level 3 daily products with 0.25° by 0.25° resolutions are aggregated into GEOS-Chem grid cells.

3.5.4 Comparisons with near-surface aerosol mass concentrations

The accuracy of the sulfate-nitrate-ammonium (SNA) aerosol simulation is in part determined by the representation of the emissions of SO₂ and NO_x and NH₃, and hence GEOS-Chem simulations with constrained emissions should provide overall an improved simulation of SNA. Figure 3.10 shows the comparison of daily near-surface SNA mass concentration from the prior and posterior GEOS-Chem simulations with measurements over Qingdao (120.34° E, 36.06° N), China. The error bars for the GEOS-Chem curves indicate the diurnal standard deviation. An overestimation in the prior model surface SNA simulations is found when comparing with observed counterparts, which shows a bias of 14.28 $\mu\text{g m}^{-3}$, RMSE of 21.84 $\mu\text{g m}^{-3}$, and correlation coefficient of 0.46. Such bias is significantly reduced to 0.34 $\mu\text{g m}^{-3}$ in the simulation with top-down constrained emissions,

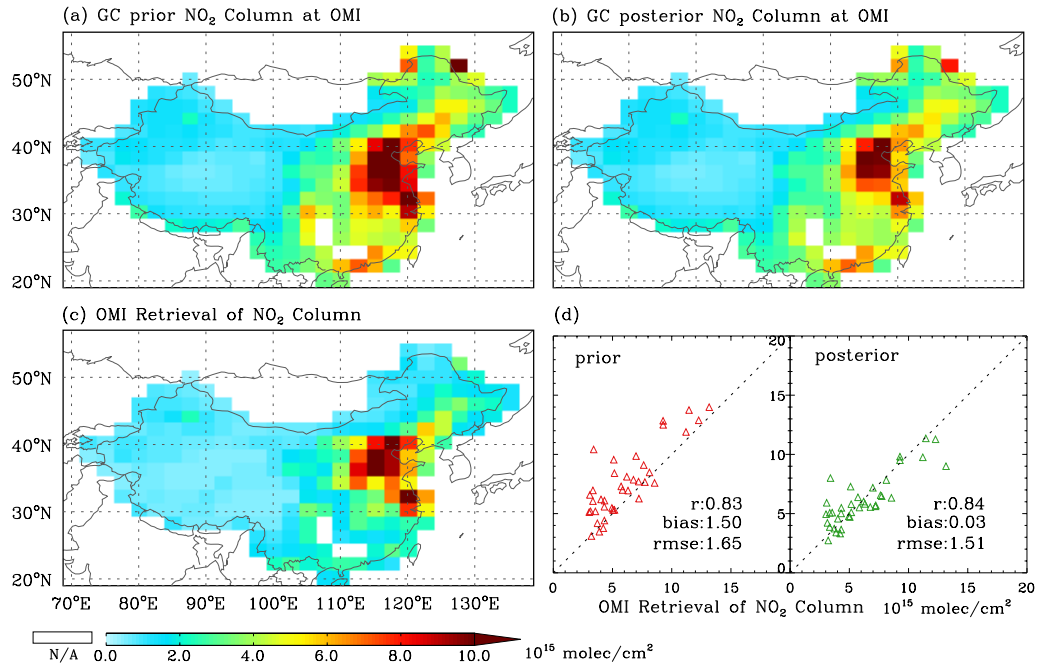


Figure 3.9: Same figure 3.7 but for comparison of the GEOS-Chem NO₂ simulation with OMI column NO₂ retrievals for the period of April 2008. The OMI tropospheric column NO₂ from Level 2 daily products with 0.25° by 0.25° resolutions are aggregated into GEOS-Chem grid cells.

along with a 50% decrease in RMSE and a 28% increase in correlation coefficient.

The mass concentration over or near the dust source regions where the anthropogenic emissions are small is most sensitive to the dust mass loading, and thus can be an indicator of the dust emissions in the first order. Figure 3.11 shows the prior and posterior GEOS-Chem surface PM₁₀ mass concentration compared with the ground-based measurements from the 2008 China-U.S. joint field experiment [Ge et al., 2010] over two the AERONET sites in Figure 3.6a-b, i.e., Zhangye (100.28° E, 39.08° N) and SACOL (204.14° E, 35.95° N), which are located on the downwind boundaries of the Gobi deserts. Based on the availability of the measurements data, comparisons are for the period of 15 – 30 April 2008. The measured surface PM₁₀ shows a strong daily variation. A strong dust event during 18–20 April can be found over both stations with PM₁₀ exceeding $400 \mu\text{g m}^{-3}$. Two additional

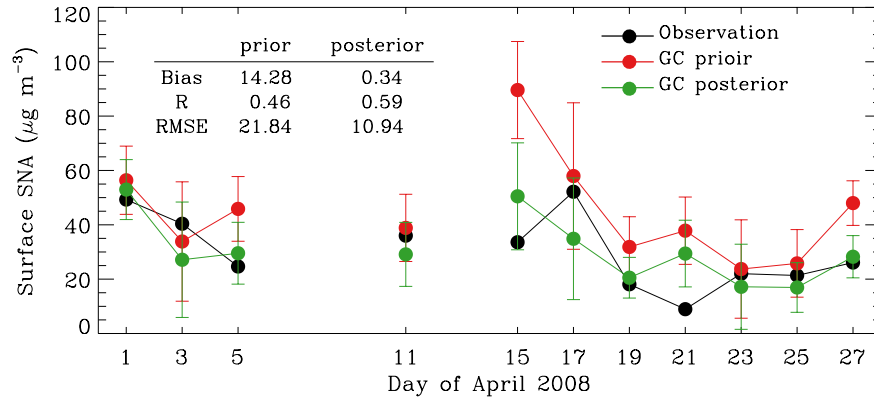


Figure 3.10: Comparison of the GEOS-Chem surface mass concentration of sulfate-nitrate-ammonium (SNA) aerosols with ground-based observations over Qingdao (120.34° E, 36.06° N), China. Discontinuity in time series is due to missing or quality filtered observations.

dust events with PM_{10} over $400 \mu\text{g m}^{-3}$ occurred during 24–26 and 29–30 April. The prior simulation generally captures the daily variation pattern but significantly overestimates the surface PM_{10} for those dust events; prior simulated PM_{10} reaches up to around $3000 \mu\text{g m}^{-3}$ over Zhangye and $1000 \mu\text{g m}^{-3}$ over SACOL for the dust events during 18–20 and 24–26 April 2008. The two-week averages show the prior simulation overestimates PM_{10} a factor of 2 over Zhangye and a factor of 1 over SACOL in the magnitude. After optimization, the relative biases in the PM_{10} simulation are reduced to about 25%. Moreover, the comparison of the time series of the PM_{10} also shows that the model value with top-down emissions has much better agreement with the measurements in terms of temporal variation.

3.5.5 Evaluation summary

A summary of evaluations of the prior and posterior model simulations is illustrated in Figure 3.12 using a Taylor diagram [Taylor, 2001]. Taylor diagram provides a statistical summary of the model performance in terms of correlation coefficients (R), centralized root-mean-square difference (RMSD), and ratio of standard deviations between model and observations (or

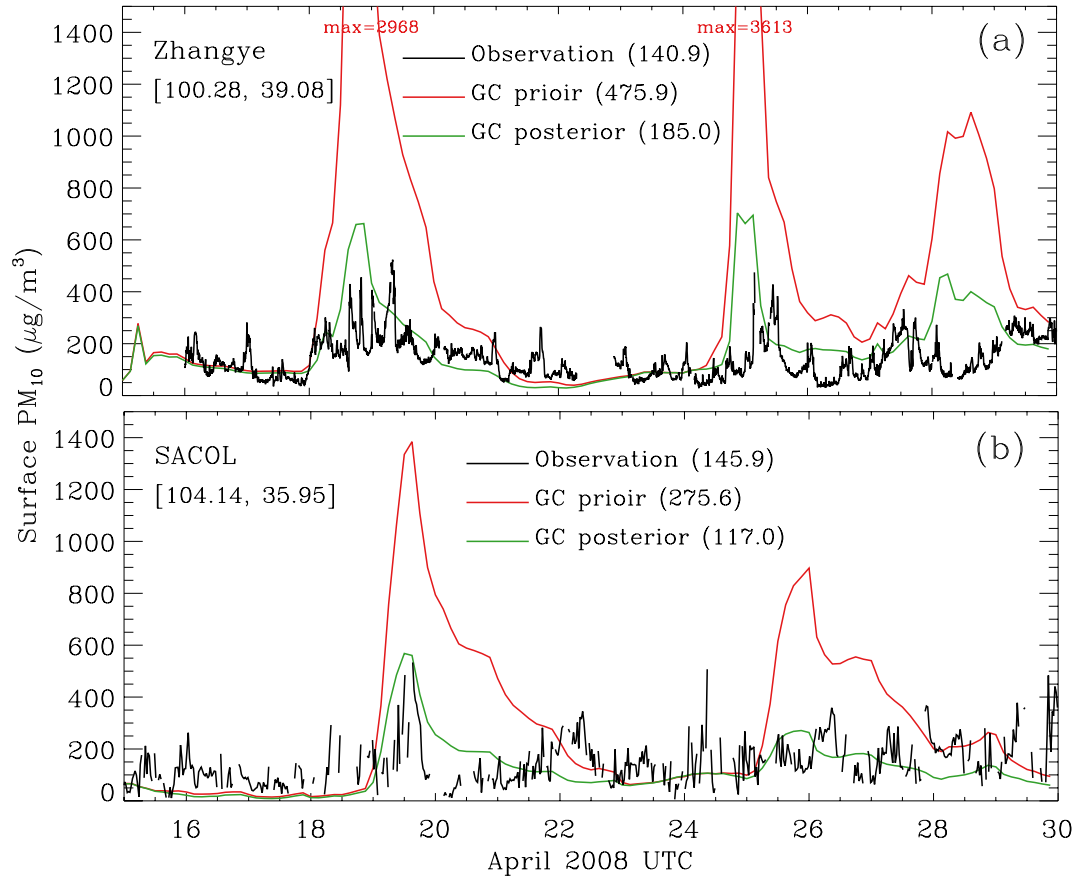


Figure 3.11: Time serial plot of the GEOS-Chem simulated surface PM_{10} concentrations by prior (red) and posterior (red) aerosol emissions compared with the *in situ* measured PM_{10} (black) over Zhangye (a) and SACOL (b) stations for 15 – 30 April 2008; also shown are the average values over same the period. Discontinuity in time series is due to missing or quality filtered observations.

normalized standard deviation, NSD). The latter two quantities reflect how well model captures the temporal or/and spatial variation of observations. In the Taylor diagram, cosine of polar angles represents R , and radius (dotted-contour) indicates NSD. Thus, the reference point (black circle) where R and NSD are unity represents observations, and the distance (dashed-contour) of certain point from which indicates the RMSD. Considering that the Taylor diagram itself is not able to show the statistical bias, we use different colors for each data points to indicate their respective relative biases. The data points labeled from 1 to 6

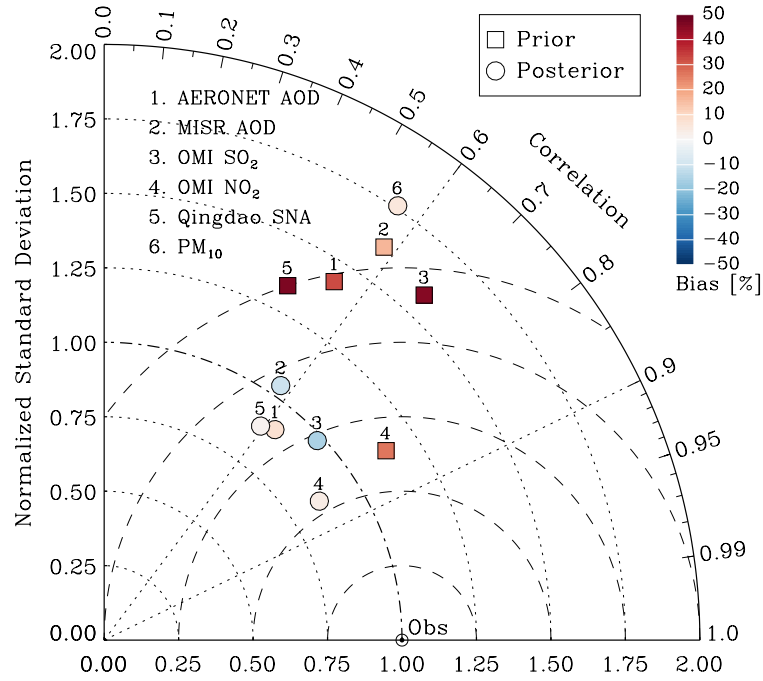


Figure 3.12: Taylor diagram for the model evaluations before (squares) and after (circles) optimization when comparing against (1) AERONET AOD at $0.55 \mu\text{m}$, (2) MISR $0.55 \mu\text{m}$ AOD, (3) OMI column SO_2 , (4) OMI column NO_2 , (5) surface SNA concentrations at Qingdao site, and (6) surface PM_{10} concentrations measured at Zhangye and SACOL sites. The color coded on each point indicates the relative bias. It should be noted that the ratio of standard deviations and correlation coefficient between prior GEOS-Chem simulated and measured surface PM_{10} over Zhangye and SACOL are 6.5 and 0.45, which makes the point number 6 for the prior simulation far beyond the range of this Taylor diagram.

indicate comparisons between model and observations of (1) AERONET AOD at $0.55 \mu\text{m}$, (2) MISR $0.55 \mu\text{m}$ AOD, (3) OMI retrievals of SO_2 Column, (4) OMI retrievals of NO_2 Column, (5) surface concentration of SNA over Qingdao, and (6) surface concentration of PM_{10} over Zhangye and SACOL, respectively. Square and circles represent the evaluations for prior and posterior GEOS-Chem simulations, respectively.

It should be noted that the NSD between prior GEOS-Chem simulated and measured surface PM_{10} during the China-U.S. joint field campaign is about 6.5 (and R of 0.45) that are significantly beyond the range of this Taylor diagram. Consequently, the square point of

number 6 is not shown in the diagram. It is clear from the Taylor diagram that the circular points (posterior simulation) are generally closer than the square points (prior simulation) to the reference point and to the unity curve of NSD, and have remarkably decreased bias. Evaluations with all those independent observations indicate a notable improvement in the model simulation, reflecting a better estimate of aerosol emissions.

3.6 Implications of Results

Interpretation of our inversion results can be from two different perspectives. First, if assuming that bottom-up anthropogenic emissions are the best estimates for their base years (mostly 2006), the reduction in the top-down emissions over China for April 2008 may indicate a decrease of emissions for April from 2006 to 2008. This conjecture is supported by the finding of significant decrease of AOD from 2006 to 2008 over the eastern China, shown both in the MODIS and MISR Level 3 gridded products (Figure 3.13), if we assume that the impact on AOD of meteorological differences between the two years is smaller than the differences in emissions. Furthermore, a slight increase of AOD over the Southeastern China (Figure 3.13) is also found to be consistent to the increase in the top-down emission estimates (Figure 3.5). In contrast to the first interpretation, the second one is that the difference of actual emissions between 2008 and their base year (2006) are smaller than the magnitude of adjustments in the optimization, and hence our results imply that the priori bottom-up emissions might be artificially overestimated. We further elucidate those two points below with a literature survey (data are summarized in Table 4).

3.6.1 SO₂

The INTEX-B inventory by Zhang et al. [2009] reported an annual production of 31.02 Tg from anthropogenic sources over China. A decrease trend of China SO₂ emissions

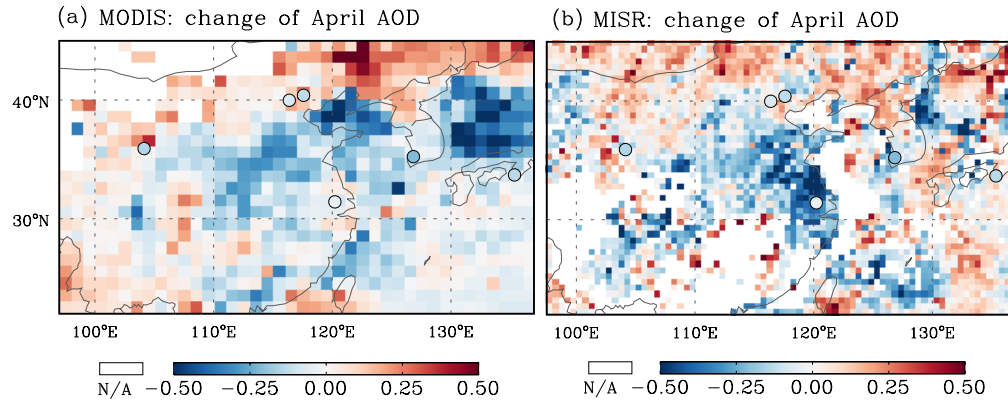


Figure 3.13: Change of April monthly $0.55 \mu\text{m}$ AOD from 2006 to 2008 from MODIS (a) and MISR (b) Level 3 daily products.

from 2006 to 2008 has been found based on bottom-up estimates by Lu et al. [2010] from 33.2 to 31.3 ($\sim 5.8\%$ decrease) Tg yr^{-1} and by China Ministry of Environmental Protection [2009] (hereafter referred to MEP-2008) from 25.9 to 23.2 Tg yr^{-1} ($\sim 10.4\%$ decrease). With OMI SO_2 retrievals, Lu et al. [2010] found the dramatic reduction of SO_2 emissions over the northern China for the same period. Similar to this study, Lu et al. [2010] also presented that the reductions is more significant over the Eastern China. They attribute some reduction to the widespread installation of flue-gas desulfurization devices in power plants, which is enforced by the China government since 2006. Evidences for the reduction trend of SO_2 emission also include the reduction of SO_2 column from 2006 observed by both SCIAMACHY and OMI satellite sensors [Lu et al., 2011]. With the same SCIAMACHY and OMI SO_2 retrievals, Lee et al. [2011] obtained top-down estimates of China SO_2 emissions, which are lower by 50% for SCIAMACHY and 30% for OMI than the INTEX-B inventory. Thus, the reduction of 33.5% in the top-down China SO_2 emissions of this work can be interpreted by the joint contribution of a decrease trend and a possible overestimation in INTEX-B bottom-up inventory.

3.6.2 NH₃

The NH₃ emissions over China have not changed much since 2000, as confirmed by the REAS inventory [Ohara et al., 2007]. Our study shows an overall decrease of 34.5% in the optimized from the TRACE-P 2000 inventory [Streets et al., 2003], which may indicate an overestimation in the TRACE-P inventory. As shown in Table 4, the total amount of the constrained NH₃ emission (0.72 Tg Mon⁻¹) for April 2008 is quite close to a recent bottom-up estimates (0.71 Tg Mon⁻¹) by Huang et al., [2012]. Huang et al., [2012] also pointed out that the TRACE-P 2000 inventory significantly overestimates the NH₃ emission by applying an overestimated emission factor across the whole country.

3.6.3 NO_x

Lin et al. [2010] constrained Chinese anthropogenic emissions of NO_x July 2008 with tropospheric NO₂ retrievals from GOME-2 and OMI instruments. They found the top-down emissions are (10–15%) lower than the *a priori* near Beijing (in agreement with results from Mijling et al. [2009]), in the northeastern provinces and along the east coast; yet they exceed the *a priori* over many inland regions. Overall, they presented a best top-down estimate of annual NO_x production is 6.8 Tg N, or 22.34 Tg NO₂, which is slightly higher than the *a priori*. While the change in NO_x emission over China remains controversy, the 18.8% difference of posterior NO_x emissions from the bottom-up still lies in the 31% uncertainty of the inventory [Zhang et al., 2009]. We argue bottom-up NO_x estimate from INTEx-B inventory could have a possible overestimation.

3.6.4 BC and OC

Major emitting sectors of BC and OC are coal and biofuel combustion by industry, residential, and transportation activities. The trend of BC and OC emissions in China during recent

years are controlled by the balance between decrease in emission factor which is pertain to improved technology and increase in coal and fuel consumptions. According to MEP-2008 [Environmental Protection Administration, 2009], the annual smoke emission in China decreased by about 17.2% from 2006 to 2008. While BC and OC emissions estimated by Lu et al. [2011] and Zhao et al. [2013] remain almost same between 2006 and 2008, Qin and Xie [2012] reported a 3.8% increase. The top-down BC emission is 0.10 Tg mon^{-1} (or 1.509 Tg yr^{-1} based on the monthly variation in INTEX-B inventory), which is smaller than that in INTEX-B, but close to estimates of 1.61 Tg yr^{-1} by Qin and Xie [2012] and 1.68 Tg yr^{-1} by Lu et al. [2011]. In terms of China OC emission estimates for 2008, Lu et al. [2011] suggested a slightly larger value (3.37 Tg yr^{-1}) while Zhao et al. [2013] indicated a smaller value (2.8 Tg yr^{-1}) than INTEX-B (3.22 Tg yr^{-1}). Our OC emission estimate (0.18 Tg mon^{-1} or 2.92 Tg yr^{-1}) is within their reported range. It is noted that the uncertainty for OC emissions is reported to be very large: 258% in INTEX-B [Zhang et al., 2009], -43% to 80% by Lu et al. [2011], and -42% to 114% in a recent study by Zhao et al. [2013].

3.6.5 Mineral dust

The 50% reduction in the posterior dust emission estimates suggests the use of DEAD mobilization scheme with GOCART source function possibly tends to produce a systematic positive bias over the Taklimakan and Gobi deserts regions over the northwestern China, even it works reasonably for the United States [Fairlie *et al.*, 2007]. Similar results have been also found in top-down dust emission estimates by MODIS aerosol retrievals [Wang et al., 2012], and constrained dust emissions by surface PM measurements [Ku and Park, 2011]. Such overestimation by the dust mobilization scheme is also reflected through comparison GEOS-Chem AOD (as in Figure 3.6) and surface PM10 concentration (as in Figure 3.11) with in situ measurements near the dust source regions.

3.7 Summary

This study presents a two-stage inversion scheme to explore the capacity of using satellite radiance for inversion of species-specific aerosol emissions. Firstly, we prepare the observational constraints of AOD using an advanced aerosol retrieval algorithm, which integrates the GEOS-Chem aerosol optical properties to the MODIS observed radiance [Wang et al., 2010]. Secondly, the adjoint of the GEOS-Chem chemical transport model is applied to statistically optimize aerosol emission estimates using these AOD retrievals. Thus, the MODIS radiances are essentially used to optimize the estimates of the emitted aerosol tracers and precursors. We illustrate our concept first with an idealized numerical experiment, and subsequently demonstrate the feasibility and practicability of the proposed scheme by applying it to optimize aerosol emission inventories over China during April 2008. Emissions of SO_2 , NH_3 , NO_x , BC and OC from anthropogenic sources, which significantly influence the aerosol simulation, are selected to be constrained at a spatial resolution of 2° by 2.5° and a monthly temporal resolution. Mineral dust production from combined natural and disturbed sources are optimized at the same spatial resolution but with a daily temporal resolution. Independent observations from both satellite remote sensing and ground-based observations are used to assess the inversion results through their comparisons with relevant GEOS-Chem simulations using prior and posterior emission estimates.

The inversion yields posterior best estimates of 1.73 Tg for SO_2 , 0.72 Tg for NH_3 , 1.38 Tg for NO_x , 0.10 Tg for BC, and 0.18 for OC from anthropogenic sources, and 8.3 Tg for combined natural and disturbed mineral dust. These show notable decreases from their counterparts in the bottom-up inventories in amount (or percentage decrease): 0.87 Tg (33.5%) for SO_2 , 0.38 Tg (34.5%) for NH_3 , 0.32 Tg (18.8%) for NO_x , 0.01 Tg (9.1%) for BC, and 0.03 Tg (15.0%) for OC. The total amount of the mineral dust emission is reduced by 56.4% from 19.02 Tg simulated by the DEAD mobilization module.

The distribution of emission scaling factors exhibits strong spatial variation for those anthropogenic-emitted tracers and considerable temporal variation for mineral dust. The use of top-down constrained emissions remarkably reduces the discrepancy between GEOS-Chem simulation and observational AOD constraints, in both spatial and temporal variation features.

Resulting posterior estimates of emissions are evaluated with independent AOD observations from surface sites (AERONET) and satellite (MISR), SO_2 and NO_2 column retrievals from satellite (OMI), and surface SNA and PM_{10} concentrations from ground-based measurements. While the prior simulation over China generally shows overestimation, the use of posterior emissions significantly enhances the consistency between simulations and those independent observations. The statistical analysis of those comprehensive comparisons summarized in the Taylor diagram shows an overall reduced bias and root-mean-square difference along with increased correlation coefficient, further confirming the improvements in the posterior simulation and the effectiveness of the presented top-down scheme.

We attribute the differences between prior and posterior aerosol emissions to the change of emitted amount from the base year of those bottom-up inventories to the study period and/or the under/over-estimations in those inventories. Through comparisons with emissions over China reported by recent studies, we find that our inversion results are consistent with following finding:

- Anthropogenic SO_2 emissions over China has been decreased by 5–10% from 2006 to 2008;
- Anthropogenic BC/OC emissions may be slightly reduced;
- Anthropogenic emissions of SO_2 and NO_x reported in the INTEx-B and NH_3 from TRACE-P inventories could have been artificially overestimated;

- The DEAD mobilization scheme combined with GOCART dust source function, even works well over the United State [?], seems to simulate mineral dust surface fluxes with a systematic positive bias.

As a first attempt to invert species-specific emissions with satellite radiance, this study has a number of limitations. Those limitations may impact the uncertainty in posterior emissions, which is supposed to be smaller than uncertainty characterizing either a priori or observational constraints [Rodgers, 2000]. While quantification of these is beyond the demonstrative purposes of this paper, we present a qualitative discussion as follows. First, in the stage of aerosol retrieval, we presume aerosol composition is unbiased, and contains errors only in the total amount. As the model inevitably has bias associating aerosol types, improvement of this assumption over regional to global scale can be obtained from innovative satellite measurements. Indeed, the radiance observations have potential information on the aerosol composition. For example, the spectral behavior of the radiance is used to discriminate smoke from mineral dust particles [King et al., 1999; Kaufman et al., 2002]. Radiances measured from multi-viewing-angle are sensitive to aerosol particle size and nonsphericity [Kahn et al., 2005]. Temporal variation and geographical location can also yield information about aerosol composition. For example, increase of AOD in semi-arid region may reflect the increase of dust, while change of AOD in the Eastern Asia may reflect the increase of industrial emission. Hence, as showed in this study, a combined use of the model-based knowledge of the dominant aerosol sources and the source-receptor relationship together with the satellite-based temporal variation of AOD at different locations can be a strong constraint for species-specific source estimates. Second, this study also assumes the sole cause of the radiance difference (or the AOD difference) is due to the uncertainty in aerosol emissions. However, other processes can contribute to the difference, e.g. aerosol transport, wet/dry deposition, diurnal variation, prescribed

aerosol physical and optical properties, and errors in the meteorological fields and radiative transfer calculation, etc. The third assumption is related to the error covariance matrices that are specified as diagonal with errors based upon literature (but that themselves may have uncertainty). To properly address these issues in future, a logical next step would be to assimilate multiple-spectral and/or multi-angle satellite radiance to the CTM. Furthermore, errors in the processes including emission, transport, and deposition and radiative transfer, should be reasonably characterized and included in the optimization.

The top-down inversion scheme using GEOS-Chem adjoint inverse modeling is a powerful tool to include observational constraints from different platforms for timely updating aerosol emissions. There is also a need of using combined tracer gas and aerosol measurements to simultaneously constrain the aerosol emissions and gas precursors. Encouraging results presented in this study reveal the potential of using aerosol observations from MODIS and MISR, SO_2 and NO_2 from OMI and other sensor, such as SCIAMACHY, in the inversion. Inclusion of those observations will undoubtedly add more information to the optimization of emission.

CHAPTER 4

OPTIMIZING DUST SOURCE PARAMETERIZATION

4.1 Introduction

Mineral dust accounts for about 40% of the global annual emissions of tropospheric aerosols [Textor *et al.*, 2006; Boucher *et al.*, 2013]. Naturally, these mineral particles are uplifted mainly by the aerolian wind erosion in arid and semiarid areas. Anthropogenic sources of mineral aerosols include road dust and mineral dust due to land changes by human activities [Tegen *et al.*, 1996, 2004; Ginoux *et al.*, 2012]. In the atmosphere, mineral dust can be transported thousands of miles away from its sources [Husar *et al.*, 2001; Toon, 2003] and influences many aspects of the Earth system through its interactions with atmospheric chemistry, solar and terrestrial radiation, clouds, and biosphere [Shao *et al.*, 2011; Ravi *et al.*, 2011; Satheesh and Krishna Moorthy, 2005; Carslaw *et al.*, 2010]. An accurate representation of dust cycle in the Earth climate model is thus critical to assess these impacts. However, significant uncertainties prevail in quantifying mineral dust sources due to the limited understanding of dust uplifting mechanisms and the lack of in situ measurements over the desert region.

Parameterization of dust entrainments in a chemistry transport model (CTM) requires knowledge of many parameters that are poorly characterized, including surface wind speed, soil moisture, soil texture, and surface state and roughness [Tegen and Fung, 1994; Ginoux *et al.*, 2001; Zender *et al.*, 2003]. Not surprisingly, recent estimates of global annual dust

emissions in CTMs span from a few hundreds to over 4000 Tg [Huneus *et al.*, 2011] and can vary by a factor as large as fifteen at regional scales for the same dust event(s) [Uno *et al.*, 2006]. An observation-based approach, therefore, is needed to reduce these large uncertainties in estimate of dust emissions and further improve the global modeling of atmospheric dust distribution and their impacts.

In the last decade, the *in situ* and satellite remote sensing observations have greatly enhanced our understanding of the spatiotemporal variations and radiative effects of dust aerosol. This is especially true for satellite retrievals that are based on multi-spectral and multi-angle radiance measurements from NASA’s Earth Observing System satellite instruments, such as MODIS and MISR, which provide daily information of aerosol optical depth (AOD) across the globe [King *et al.*, 1999; Kaufman *et al.*, 2002; Martonchik *et al.*, 2009]. The MODIS “deep blue” (DB) aerosol retrievals [Hsu *et al.*, 2006, 2013] further made the aerosol information over bright deserts available. On the other hand, *in situ* observations (e.g. AERONET [Holben *et al.*, 1998]) and experiment campaigns, even though sparse in their temporal and spatial coverage, usually have advantages in their accuracy, and thus are valuable for validating satellite aerosol products and model simulations.

In this dissertation, I thus seek to contribute an improved understanding of the dust emissions through (i) . . . , (ii) . . . , and (iii).

4.2 Necessary Implementations

4.2.1 Development of the wind speed distribution

In order to incorporate the variability of wind speed due to the subgrid scale circulations, we introduce a probability density function (PDF) of the wind speed within each grid box. The dust emission is computed according to the fraction of the PDF that exceeds the threshold

value:

$$E_d = \int_{u_{*l}}^{\infty} E(u_*) p(u_*) du_*. \quad (4.1)$$

Where $E(u_*)$ is the emission as a function of the surface wind friction velocity, and $p(u_*)$ is the PDF of u_* within the grid box.

The PDF for surface wind speeds can be represented by a Weibull distribution [Justus et al., 1978] and has been used in recent studies [e.g., Grini and Zender, 2004; Grini et al., 2005; Ridley et al., 2013] to characterize the subgrid dust emissions. The PDF of a Weibull random variable x is described by a shape factor k and a scale factor c :

$$p(x; c, k) = \frac{k}{c} (x/c)^{k-1} \exp \left[-(x/c)^k \right], \text{ for } x > 0. \quad (4.2)$$

One of the advantages in using the Weibull PDF is that it is analytically integrable with the cumulative distribution function:

$$P(x \leq x_1; c, k) = 1 - \exp \left[-(x/c)^k \right]. \quad (4.3)$$

Based on above cumulative function, we cut off wind speeds with a minimum and a maximum wind speed to retain the central 98% of the wind PDF. As a result, the lower and upper limits of wind speed are respectively:

$$x_l = c \left[-\ln 0.99 \right]^{\frac{1}{k}} \quad (4.4)$$

$$x_u = c \left[-\ln 0.01 \right]^{\frac{1}{k}} \quad (4.5)$$

Parameters k and c can be estimated from the statistical mean \bar{x} and variance σ^2 (of x),

since they are related to \bar{x} and σ^2 :

$$\bar{x} = c\Gamma(1 + 1/k) \quad (4.6)$$

$$\sigma^2 = c^2 [\Gamma(1 + 2/k) - \Gamma^2(1 + 1/k)] \quad (4.7)$$

Where $\Gamma()$ is a gamma function. According to Justus et al. [1978], k and c can be best estimated by:

$$k = (\sigma/\bar{x})^{-1.086} \quad (4.8)$$

$$c = \bar{x}[\Gamma(1 + 1/k)]^{-1} \quad (4.9)$$

Thus, the only parameter that must be supplied beyond the mean wind speed is the variance (σ^2) of subgrid wind speeds within the grid box. Cakmur et al [2004] calculated the σ^2 by incorporating information from the parameterizations of the planetary boundary layer along with dry and moist convection. Here, we follow Grini and Zender [2004] and Grini et al [2005] that assumed an approximation of k based on Justus et al. [1978]:

$$k = 0.94u_*^{\frac{1}{2}} \quad (4.10)$$

Finally, the dust emission flux is calculated by

$$E_{d,j} = A_m S \alpha \left(\sum_{i=1}^3 M_{i,j} \right) \frac{c_s \rho}{g} \int_{u_{*t}}^{u_{*u}} u_*^b \left(1 - \frac{u_{*t}}{u_*} \right) \left(1 + \frac{u_{*t}}{u_*} \right)^2 p(u_*) du_*. \quad (4.11)$$

Where u_{*u} is the upper limit of wind speed determined by equation (4.5).

4.2.2 AOD observation operator

Inversion of dust emissions from AOD observations requires an observation operator that relates AOD to emission. Such observation operator of this study comprises a GEOS-Chem forward model that simulates aerosol concentrations with input of emissions and an AOD operator that computes AOD from aerosol concentrations. AOD at any wavelength is calculated from the sum of AODs of each component assuming external mixing state of aerosol particles:

$$\tau_A = \sum_{i=1}^{n_{\text{spec}}} \beta_{\text{ext}_i} c_i \frac{3c_i Q_{\text{ext}_i}}{4\rho_i r_{\text{eff}_i}} \quad (4.12)$$

where n_{spec} is the number of aerosol components, c_i is the aerosol mass concentration of the i th component, and β_{ext_i} is the mass extinction efficiency. β_{ext_i} is related to the

4.2.3 Adjoint for Dust Flux Parameterization

In simple, The dust emission flux considering subgrid wind speeds in equation (4.11) can be written

$$E_{d,j} = C_j S' \int_{u_{*t}}^{u_{*u}} Q_s(u_*, u_{*t}, b) p(u_*) du_*, \quad (4.13)$$

where $S' = S\alpha$, and $C_j = A_m \sum_{i=1}^3 M_{i,j}$. We combine the erodibility S and sandblasting factor α , because both of them not only are related to the soil texture but also describe the strength efficiency of dust emission. Given the the state of land surface and the properties of surface soil, the dust emission is a function of S' , b , and u_{*t} .

Here we implement the adjoint calculation for three parameters, i.e., S' , b , and u_{*t} . This implementation requires the partial derivatives of $E_{d,j}$ with respect to these parameters (when $u_* \geq u_{*t}$):

$$\frac{\partial E_{d,j}}{\partial S'} = \frac{E_{d,j}}{S'}, \quad (4.14)$$

$$\frac{\partial E_{d,j}}{\partial b} = C_j S' \int_{u_{*t}}^{u_{*u}} \frac{\partial Q_s}{\partial b} p(u_*) du_*, \quad (4.15)$$

$$\frac{\partial E_{d,j}}{\partial u_{*t}} = C_j S' \int_{u_{*t}}^{u_{*u}} \frac{\partial Q_s}{\partial u_{*t}} p(u_*) du_*. \quad (4.16)$$

These gradients of Q_s in equations (4.15 and 4.16) can be calculated by

$$\frac{\partial Q_s}{\partial b} = Q_s(u_*, u_{*t}, b) \ln u_* \quad (4.17)$$

$$\frac{\partial Q_s}{\partial u_{*t}} = \frac{c_s \rho}{g} u_*^b \left[\frac{1}{u_*} - \frac{2u_{*t}}{u_*^2} - \frac{3u_{*t}^2}{u_*^3} \right] \quad (4.18)$$

4.3 Constraints from Multi-Satellite Observations

4.4 Experiment Design

4.5 Constrained Dust Emission Scheme

4.6 Validations

4.7 Summary

CHAPTER 5

SUMMARY AND OUTLOOK

5.1 Summary of the Dissertation

5.2 Main Conclusions of This Work

5.3 Outlook and Future Work

APPENDIX A

ABBREVIATIONS AND ACRONYMS

APPENDIX B

SYMBOLS

REFERENCES

- Boucher, O., et al. (2013), *Clouds and Aerosols. In Climate Change 2013: The Physical Science Basis. Contribution of Working Group I to the Fifth Assessment Report of the Intergovernmental Panel on Climate Change [Stocker T.F., et al. (eds.)]*, p. 571–658, Cambridge University Press, Cambridge, United Kingdom and New York, NY, USA. [4.1](#)
- Burrows, S. M., T. Butler, P. Jockel, H. Tost, A. Kerkweg, U. Poschl, and M. G. Lawrence (2009), Bacteria in the global atmosphere. part 2: Modeling of emissions and transport between different ecosystems, *Atmospheric Chemistry and Physics*, 9(23), 9281–9297. [1.1](#)
- Byrd, R. H., P. Lu, J. Nocedal, and C. Zhu (1995), A limited memory algorithm for bound constrained optimization, *SIAM Journal on Scientific Computing*, 16, 1190–1208. [2.1](#)
- Carslaw, K. S., O. Boucher, D. V. Spracklen, G. W. Mann, J. G. L. Rae, S. Woodward, and M. Kulmala (2010), A review of natural aerosol interactions and feedbacks within the earth system, *Atmos. Chem. Phys.*, 10(4), 1701–1737, aCP. [4.1](#)
- Fairlie, D. T., D. J. Jacob, and R. J. Park (2007), The impact of transpacific transport of mineral dust in the united states, *Atmospheric Environment*, 41(6), 1251–1266, doi: DOI: 10.1016/j.atmosenv.2006.09.048. [3.4](#), [3.6.5](#)
- Ginoux, P., M. Chin, I. Tegen, J. M. Prospero, B. Holben, O. Dubovik, and S.-J. Lin (2001), Sources and distributions of dust aerosols simulated with the gocart model, *J. Geophys. Res.*, 106(D17), 20,255–20,273. [4.1](#)
- Ginoux, P., J. M. Prospero, T. E. Gill, N. C. Hsu, and M. Zhao (2012), Global-scale attribution of anthropogenic and natural dust sources and their emission rates based on modis deep blue aerosol products, *Reviews of Geophysics*, 50(3), RG3005. [4.1](#)
- Griffin, D., V. Garrison, J. Herman, and E. Shinn (2001), African desert dust in the caribbean atmosphere: Microbiology and public health, *Aerobiologia*, 17(3), 203–213. [1.1](#)

- Hansen, P. C. (1998), *Rank-Deficient and Discrete Ill-Posed Problems: Numerical Aspects of Linear Inversion*, Soc. for Ind. and Appl. Math., Philadelphia, Pa. [2.1](#)
- Henze, D. K., A. Hakami, and J. H. Seinfeld (2007), Development of the adjoint of geos-chem, *Atmos. Chem. Phys.*, 7(9), 2413–2433. [1.1](#), [2.3](#)
- Henze, D. K., J. H. Seinfeld, and D. T. Shindell (2009), Inverse modeling and mapping us air quality influences of inorganic pm2.5 precursor emissions using the adjoint of geos-chem, *Atmos. Chem. Phys.*, 9(16), 5877–5903. [2.3](#)
- Holben, B. N., et al. (1998), Aeronet - a federated instrument network and data archive for aerosol characterization, *Remote Sensing of Environment*, 66(1), 1–16. [4.1](#)
- Hsu, N. C., T. Si-Chee, M. D. King, and J. R. Herman (2006), Deep blue retrievals of asian aerosol properties during ace-asia, *Geoscience and Remote Sensing, IEEE Transactions on*, 44(11), 3180–3195. [4.1](#)
- Hsu, N. C., M. J. Jeong, C. Bettenhausen, A. M. Sayer, R. Hansell, C. S. Seftor, J. Huang, and S. C. Tsay (2013), Enhanced deep blue aerosol retrieval algorithm: The second generation, *Journal of Geophysical Research: Atmospheres*, 118(16), 9296–9315. [4.1](#)
- Huneeus, N., et al. (2011), Global dust model intercomparison in aerocom phase i, *Atmos. Chem. Phys.*, 11(15), 7781–7816. [4.1](#)
- Husar, R. B., et al. (2001), Asian dust events of april 1998, *J. Geophys. Res.*, 106(D16), 18,317–18,330. [4.1](#)
- Jiang, Z., D. B. A. Jones, M. Kopacz, J. Liu, D. K. Henze, and C. Heald (2011), Quantifying the impact of model errors on top-down estimates of carbon monoxide emissions using satellite observations, *Journal of Geophysical Research: Atmospheres*, 116(D15), D15,306. [2.3](#)
- Jickells, T. D., et al. (2005), Global iron connections between desert dust, ocean biogeochemistry, and climate, *Science*, 308(5718), 67–71. [1.1](#)
- Kaufman, Y. J., D. Tanre, and O. Boucher (2002), A satellite view of aerosols in the climate system, *Nature*, 419, 215 – 223. [4.1](#)

- King, M. D., Y. J. Kaufman, D. Tanre, and T. Nakajima (1999), Remote sensing of tropospheric aerosols from space: Past, present, and future, *Bulletin of the American Meteorological Society*, 80(11), 2229–2259. [4.1](#)
- Kopacz, M., D. J. Jacob, D. K. Henze, C. L. Heald, D. G. Streets, and Q. Zhang (2009), Comparison of adjoint and analytical bayesian inversion methods for constraining asian sources of carbon monoxide using satellite (mopitt) measurements of co columns, *J. Geophys. Res.*, 114(D4), D04,305. [2.3](#)
- Kopacz, M., et al. (2010), Global estimates of co sources with high resolution by adjoint inversion of multiple satellite datasets (mopitt, airs, sciamachy, tes), *Atmos. Chem. Phys.*, 10(3), 855–876. [2.3](#)
- Kopacz, M., D. L. Mauzerall, J. Wang, E. M. Leibensperger, D. K. Henze, and K. Singh (2011), Origin and radiative forcing of black carbon transported to the himalayas and tibetan plateau, *Atmos. Chem. Phys.*, 11(6), 2837–2852. [2.3](#)
- Martonchik, J. V., R. A. Kahn, and D. J. Diner (2009), *Retrieval of aerosol properties over land using MISR observations*, Springer, Berlin. [4.1](#)
- Parrington, M., et al. (2012), The influence of boreal biomass burning emissions on the distribution of tropospheric ozone over north america and the north atlantic during 2010, *Atmospheric Chemistry and Physics*, 12(4), 2077–2098. [2.3](#)
- Ravi, S., et al. (2011), Aeolian processes and the biosphere, *Reviews of Geophysics*, 49(3), RG3001. [4.1](#)
- Rodgers, C. D. (2000), *Inverse Methods for Atmospheric Sounding: Theory and Practice*, World Scientific, Singapore. [2.1](#)
- Satheesh, S. K., and K. Krishna Moorthy (2005), Radiative effects of natural aerosols: A review, *Atmospheric Environment*, 39(11), 2089–2110. [4.1](#)
- Shao, Y., et al. (2011), Dust cycle: An emerging core theme in earth system science, *Aeolian Research*, 2(4), 181–204. [4.1](#)
- Streets, D. G., et al. (2003), An inventory of gaseous and primary aerosol emissions in asia in the year 2000, *J. Geophys. Res.*, 108(D21), 8809. [1.1.1](#)

- Tegen, I., and I. Fung (1994), Modeling of mineral dust in the atmosphere: Sources, transport, and optical thickness, *J. Geophys. Res.*, 99(D11), 22,897–22,914. [4.1](#)
- Tegen, I., A. A. Lacis, and I. Fung (1996), The influence on climate forcing of mineral aerosols from disturbed soils, *Nature*, 380(6573), 419–422. [4.1](#)
- Tegen, I., M. Werner, S. P. Harrison, and K. E. Kohfeld (2004), Relative importance of climate and land use in determining present and future global soil dust emission, *Geophys. Res. Lett.*, 31(5), L05,105. [4.1](#)
- Textor, C., et al. (2006), Analysis and quantification of the diversities of aerosol life cycles within aerocom, *Atmos. Chem. Phys.*, 6(7), 1777–1813. [4.1](#)
- Toon, O. B. (2003), Atmospheric science: African dust in florida clouds, *Nature*, 424(6949), 623–624, 10.1038/424623a. [4.1](#)
- Uno, I., et al. (2006), Dust model intercomparison (dmip) study over asia: Overview, *J. Geophys. Res.*, 111(D12), D12,213. [4.1](#)
- Wecht, K. J., D. J. Jacob, S. C. Wofsy, E. A. Kort, J. R. Worden, S. S. Kulawik, D. K. Henze, M. Kopacz, and V. H. Payne (2012), Validation of tes methane with hippo aircraft observations: implications for inverse modeling of methane sources, *Atmospheric Chemistry and Physics*, 12(4), 1823–1832. [2.3](#)
- Zender, C. S., H. Bian, and D. Newman (2003), Mineral dust entrainment and deposition (dead) model: Description and 1990s dust climatology, *J. Geophys. Res.*, 108(D14), 4416. [3.4](#), [4.1](#)
- Zhu, C., R. H. Byrd, P. Lu, and J. Nocedal (1994), L-bfgs-b: a limited memory fortran code for solving bound constrained optimization problems, *Technique report*, Northwestern University. [2.1](#)
- Zoogman, P., et al. (2011), Ozone air quality measurement requirements for a geostationary satellite mission, *Atmospheric Environment*, 45(39), 7143 – 7150. [2.3](#)

LIST OF PUBLICATIONS

List my publication here